DEPARTMENT OF PHYSICS
UNIVERSITY OF JYVÄSKYLÄ
RESEARCH REPORT No. 3/2016

The effect of steric hindrance on the packing of elongated objects

Axel Ekman

Academic Dissertation
for the Degree of
Doctor of Philosophy

To be presented, by permission of the
Faculty of Mathematics and Natural Sciences
of the University of Jyväskylä,
for public examination in Auditorium FYS1 of the
University of Jyväskylä on February 22nd, 2016
at 12 o'clock noon

JYVÄSKYLÄ, FINLAND 2016

ABSTRACT

Fibres of various materials can be deposited to form planar mats of fibres. These kinds of structures have gained substantial attention owing to their direct relation to both large industrial fields, such as paper and nonwovens, and biological structures, such as natural networks of fibrin, actin and collagen. In addition, similar structures are important in new emerging fields such as flexible electronics and tissue engineering. The physical properties of these structures are directly related to the connectivity of the network, thus a thorough understanding of the contact formation of the system is of great importance from both a scientific viewpoint as well as for its application in the engineering of such structures.

In this Thesis we extend on the work regarding the structure of such random networks by considering, in more detail, the effect of the steric hindrance between the constituents. Most notably, we find that even if the effect on averaged properties in many cases can be negligible, its effect on statistical properties of the contact formation remains substantial even for dilute systems.

Keywords: random networks, numerical simulation, porous material, X-ray tomography.

Author
Axel Ekman
Department of Physics
University of Jyväskylä
Jyväskylä, Finland

Supervisor
Prof. emer. Jussi Timonen
Department of Physics
University of Jyväskylä
Jyväskylä, Finland

Reviewers
Prof. Seth Fraden
Department of Physics
Brandeis University
Waltham, USA

Dr. Ari Puurtinen
Lappeenranta University of Technology
Lappeenranta, Finland

Opponent
Prof. Alex Hansen
Department of Physics
Norwegian University of Science and Technology
Trondheim, Norway

ISSN 0075-465X
ISBN 978-951-39-6531-0 (nid.)
ISBN 978-951-39-6532-7 (PDF)

YHTEENVETO (FINNISH SUMMARY)

Tasomaisista kuituverkoista koostuvia materiaaleja on runsaasti. Ne ovat herättäneet kiinnostusta varsinkin suurilla teollisuusaloilla, kuten paperi- ja kuitukangasteollisuudessa, sekä biologian alalla, etenkin koskien luonnon aktiini-, fibriini- ja kollageenirakenteita. Vastaavanlaisia rakenteita hyödynnetään myös nousevilla aloilla, kuten esimerkiksi joustavassa elektroniikassa ja kudosteknologiassa. Yllämainittujen materiaalien fysikaaliset ominaisuuden riippuvat voimakkaasti verkon kuitujen välisistä kontakteista, joten tarkka tieto kontaktien määrästä ja jakautumisesta on keskeinen tekijä materiaalien ominaisuuksien ennustamisessa.

Tässä väitöskirjatutkimuksessa laajennetaan nykyistä ymmärrystä satunnaisverkkojen kontakteista ja tarkastellaan steerisen esteen vaikutusta kontaktien muodostumisessa. Tärkeimpänä tuloksena voidaan todeta, aikaisempia tietoja tarkentaen, että steerisen esteen vaikutus on havaittavissa myös hyvin harvarakenteisissa verkoissa. Tämä vaikutus näkyy kontaktien tilastollisia ominaisuuksia tarkasteltaessa, jolloin huomataan selkeä kontaktien välinen korrelaatio.

Asiasanat: satunnaiset verkot, numeerinen simulaatio, huokoinen aine, röntgentomografia.

ACKNOWLEDGEMENTS

The work reported in this Thesis has been carried out during the years 2010–2015 at the Department of Physics at the University of Jyväskylä, Finland. I gratefully acknowledge financial support from the Academy of Finland, Jane and Aatos Erkko Foundation and Stora Enso. I also thank my pre-examiners Prof. Seth Fraden and Dr Ari Puurtinen for their effort and for providing valuable comments on the original manuscript.

I owe a debt of gratitude to my supervisor, Prof. emer. Jussi Timonen, whom it has been a pleasure to work with. Seldom does one receive guidance with such proficiency and patience and I consider these years as an invaluable experience.

The scientific journey is not an easy one to take alone, and thus I wish to express my gratitude to my co-authors: Ahmad Al-Qararah, Kaj Backfolk, Nikolai Beletksi, Tuomo Hjelt, Jukka Ketoja, Harri Kiiskinen, Antti Koponen and Keijo Mattila, who have all helped me along the way. Especially I thank Arttu Miettinen for his never-ending curiosity and resilience with my seemingly endless array of questions, Tuomas Turpeinen for teaching me essentially everything I know about image processing and Tuomas Tallinen for offering seasoned academic guidance.

The work involved for this Thesis would not have been as pleasant if not for the great atmosphere that was provided by the numerous friends and colleagues at the Department. This includes lively and 'topical' lunch discussions due to Topi Kähärä, Jukka Kuva and Vantte Kilappa and numerous joint conference attendances with the Holvi collaboration.

The foundation of my work stem from times long before my academic adventure, and although my lovingly scrutinous Mother and sagacious Father both have their imprint directly on this Thesis, I feel that I am more indebted for their many years of care and upbringing.

Finally, my deepest thanks goes to my dear wife Heljä for endurance and support throughout these years, and my daughter Luna for conditioning me for the necessary peculiar working hours.

Jyväskylä
5th February 2016
Axel Ekman

LIST OF PUBLICATIONS

I A. Ekman, A. Miettinen, T. Turpeinen, K. Backfolk, and J. Timonen. The number of contacts in random fibre networks. *Pulp and paper, 27(2):270–276*, 2012.

II A. Ekman, A. Miettinen, T. Tallinen, and J. Timonen. Contact Formation in Random Networks of Elongated Objects. *Physical Review Letters, 113(26):268001*, 2014.

III A. M. Al-Qararah, A. Ekman, T. Hjelt, J. Ketoja, H. Kiiskinen, A. Koponen, J. Timonen. A unique microstructure of the fiber networks deposited from foam–fiber suspension. *Colloids and Surfaces A: Physicochemical and Engineering Aspects,482:544–553*, 2014.

IV A. M. Al-Qararah, A. Ekman, N. Beletski, T. Hjelt, H. Kiiskinen, J. Timonen, J. Ketoja. Porous structure of fiber networks formed by a foaming process: a comparative study of different characterization techniques. *Submitted*, 2015.

V A. Ekman, T. Tallinen, and J. Timonen. Excess of end contacts in networks of randomly-packed finite rods. *Submitted*, 2015.

VI A. Koponen, A. Ekman, K. Mattila, A. M. Al-Qararah, and J. Timonen. The effect of void structure on the permeability of fibrous networks. *Submitted*, 2015.

The author is the principal author of publication **I**, **II**, and **V** and was responsible for the μCT imaging, image analysis, and partial data analysis in **III**, **IV**, and **VI**. In addition, he has contributed to the following relevant publications:

VII T. Karppinen, R. Montonen, M. Määttänen, A. Ekman, M. Myllys, J. Timonen, and E. Hæggström. Evaluating pulp stiffness from fibre bundles by ultrasound. *Measurement Science and Technology, 23(6):065603*, 2012

VIII A. Miettinen, A. Ekman, G. Chinga-Carrasco, and M. Kataja. Measuring intrinsic thickness of rough membranes: application to nanofibrillated cellulose films. *Journal of Materials Science, 50(21):6926–6934*, 2015

CONTENTS

1 INTRODUCTION

Randomly packed materials are ubiquitous in our daily lives. Examples of such range from naturally occurring piles, such as the soil we stand on, to every day items such as the storage of dry foods. Stochastic structures are also present in a wide range of practical application such as paper products, packaging materials, tissues and filters. These are all examples of materials made from smaller constituents, where the collective behaviour of the bulk is drastically different from the behaviour of the single constituent.

One could say the simplest form of these random packings are those of granular matter. They are collections of non-thermal particles, i.e., large enough so that thermal fluctuations have a negligible effect on the system. Even though, at a glance, these kinds of materials seem very simple (macroscopic classical dynamics) the same collection of particles can express behaviour of a solid, fluid or gas (Jaeger et al., 1996) depending on the environment. Granular matters also display a wide range of collective complex behaviours such as jamming (Corwin et al., 2005; Song et al., 2008; Ellenbroek et al., 2009), self-organized criticality (Bak et al., 1988; Frette et al., 1996) and load-bearing force chains (Cates et al., 1998; Majmudar and Behringer, 2005). Increasing the aspect ratio of the particles is known to have an effect on the packing of these materials and e.g. piles of long aspect ratio rods form entangled states that are very different from piles of sand (Philipse, 1996; Desmond and Franklin, 2006; Blouwolff and Fraden, 2006) being more robust and even withstanding stretching.

By adding flexibility to the elongated particles, we arrive on the field of macroscopic fibrous materials. Fibre networks of this kind have also been studied extensively owing to their obvious application in big industrial fields, such as nonwovens (Pan et al., 2007) and paper (Niskanen et al., 1997). These materials include common household items such as paper, packaging materials, absorptive tissue, various filters and insulating materials. With only a slight difference in the materials used these types of structures can have highly different properties depending on their end use including wetting behaviour, permeability, thermal

conductivity, elastic stiffness and strength properties.

On an even smaller scale fibrous networks appear in biological structures (Fletcher and Mullins, 2010), both in intracellular structures such as the cytoskeleton (Medalia et al., 2002) and extracellular networks of e.g. fibrin (Baradet et al., 1995; Jockenhoevel and Flanagan, 2011) or collagen (Yurchenco and Ruben, 1987). These biological networks are made of semi-flexible filaments, and are in a length scale where thermal effects start to play a role. The materials are known to be non-linear in their elastic response even for relatively low strain rates (Storm et al., 2005; Broedersz et al., 2008). Numerical simulation also show that these kinds of networks show a wide range of behaviour depending on the length scales and geometry of the structure (Head et al., 2003; Wilhelm and Frey, 2003), an effect which has also been reproduced on lattice based systems (Broedersz et al., 2011, 2012). Details in the connectivity also play a large role in the elastic response of the network (Huisman et al., 2007). A recent surge of interest for random networks has also risen owing to the applications of nanotubes in both composite materials and as deposited films (Snow et al., 2003; Du et al., 2004; Hu et al., 2004; Dalmas et al., 2006; Cao and Rogers, 2009; Hu et al., 2010; Sangwan et al., 2012).

The common factor in all these materials is that the interesting behaviour arises from their interaction with each other. These interactions, in the static case, are described by contacts (stabilized by either mechanical or chemical effects) and give rise to the collective behaviour of the network, making the understanding of the contact formation a fundamental link to the understanding of the macroscopic behaviour of the material. Although the theoretical groundwork for modelling the structures as random networks is well developed, a subject that has remained unsettled is the effect of steric hindrance. Even recent reviews of the subject (Picu, 2011), although giving a very comprehensive summary of the current understanding of random fibre networks, do not address the this effect thoroughly.

The main objective of this work was to investigate the effect of steric hindrance on the structure of randomly deposited networks. As the physical properties depend on the both mean and distributional properties of the network, the aim was to investigate both. The distributional part was addressed by considering an abstract model for sterically hindered contact formation in a linear space. This resulted in candidate distributions for the segment length in actual networks. To address the question of global averaged properties in these networks we turned to numerical methods and developed a dynamic model of flexible rods.

This Thesis is structured as follows: we give an introduction to random networks in Chapter 2 and to tomographic x-ray imaging in Chapter 3. The main body of our work is introduced in Chapter 4, where we introduce our model for steric hindrance. Chapter 5 is reserved for numerical and experimental methods and the consequential results are presented in Chapter 6. A brief summary and outlook is given in Chapter 7.

2 UNCORRELATED NETWORKS

Taking into account all the intricate details in the formation of a fibrous structure is an extremely difficult task. Taking into account all the physical and geometrical details of its constituents when trying to solve physical properties of the material is also more often not possible. Fibrous structures are often thought of as a network of their constituents i.e. they are formed by a collection of fibres confined in the same space and which are connected in some way. By this notion we have already decoupled two things: the geometry and the connectivity. This is a common procedure in many fields i.e. breaking down problems into smaller pieces, which can be individually solved and later combined for relevant information.

A good starting point is that of a randomly formed network, such that a random variable X describing the relevant positional, orientation and geometrical features of a single constituent is taken independent from a multivariate distribution $f_X(x)$[1]. This reduces the formation of the network to a problem of stochastic geometry. A simple, yet powerful, example of such network is the random isotropic network of line segments (fig. 1a). By drawing N lines of length L onto $\mathbb{R}^2$ we have a family of well defined stochastic networks controlled by only two parameters, the length scale L and a process density $\rho_f = N/L^2$, yet these structures predict many features of realistic materials and has been the underlying model for numerous works on random networks e.g. (Åström et al., 2000a,b; Cheng et al., 2001; Wilhelm and Frey, 2003; Yi et al., 2004; Berhan et al., 2004; Wu and Dzenis, 2005; Heussinger and Frey, 2006; DiDonna and Levine, 2006; Heussinger et al., 2007).

The mathematical problem of random lines can be dated back to the Buffon needle problem, and the general solutions to the problem of crossing lines can be dated back to the 19th century by Crofton (1868) and Sylvester (1890). However, studies addressing the problem of random network structures appear much later. Although Goudsmit (1945) considered the polygons formed by infinite lines, the

[1] Note that not all uncorrelated random processes are independent, but all independent processes are uncorrelated. We choose to call these networks uncorrelated as the term independent might confuse readers to assume they are non-interacting.

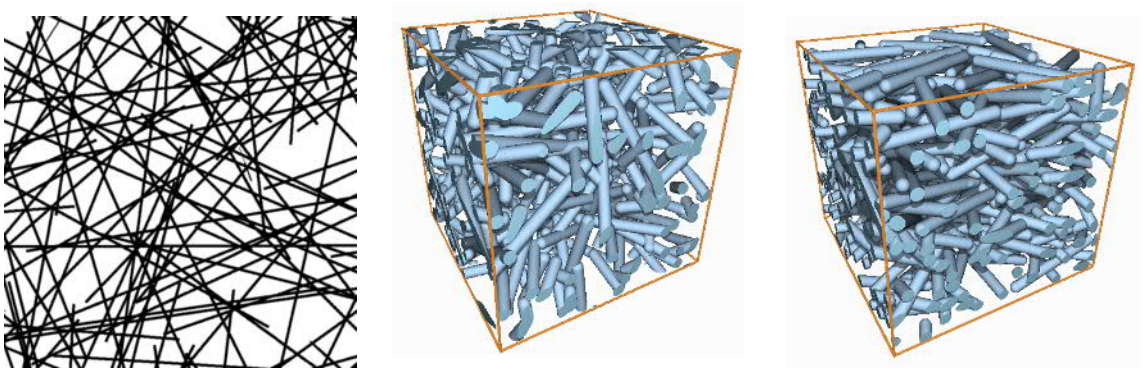

(a) 2D line (b) 3D isotropic (c) deposition

FIGURE 1 Illustrations of three different kinds of a network. A 2D (zero-width) deposited network (a), a network of isotropically distributed cylinders (b) and a deposited network of fibres with non-zero width (c).

works of Kallmes and Corte (1960) are regarded as the pioneering in modeling the structure of fibrous materials as random (2D) line networks. Kallmes and Corte (1960) derived a wide number of properties for these kinds of networks, most notably the number of contacts and the free fibre length between them, i.e. the segment length. Further work was done by Miles (1964) on the both distributional and mean properties of the formed polygons. Miles (1964) is also one of the first to consider the effect of non-zero width. One may find it surprising that the first considerations of network structure in three dimensions (3D) appeared earlier and was made by van Wyk (1946) in his seminal publication on the compressibility of wool. Further work on uncorrelated 3D networks (fig. 1b) have been carried out by e.g. Komori and Makishima (1977), Dodson (1996) and Toll (1998).

Theoretical estimations of structural properties have been especially important in the study of paper, which have been nicely summarized by Deng (1994). In this field, the measure of choice is usually relative bonding area (RBA)[2]. The reasoning behind this originates from the difficulty in measuring a single contact directly, requiring for other methods to address the relationship between network connectivity and its mechanical properties (Ingmanson and Thode, 1959), and many authors address the network properties in this light both theoretically (Sampson, 2003, 2004; Sampson and Sirviö, 2005; He et al., 2007) and experimentally (Batchelor and He, 2005; Batchelor et al., 2008).

In this chapter we summarise some general features of uncorrelated random networks relevant to our work and link them to properties of the physical systems. A brief note on uncorrelated models is given at the end of the chapter.

[2] Many also use the term fractional contact area (FCA), distinguishing it from RBA because not all contacts between fibres bear any load.

2.1 Properties of random networks

Regardless of the exact process of network formation, there are some properties which we can define to hold true for all networks of our interest. Consider placing a fibre in contact with an existing network so that it makes C contacts. Including the dangling ends, the fibre itself will be divided into $C + 1$ segments, and all new contacts divide an existing segment into two. In total every added fibre produces, on the average, $2\langle C\rangle + 1$ new segments, where the brackets denote an average value. A network of N_f fibres thus has a total of $N_\mathrm{s} = 2N_\mathrm{c} + N_\mathrm{f}$ segments, where N_c is the total number of contacts. Correspondingly,

$$\rho_\mathrm{s} = 2\rho_\mathrm{c} + \rho_\mathrm{f} \tag{1}$$

for the number densities $\rho_\mathrm{c,f,s} = N_\mathrm{c,f,s}/V$ in a volume V. Global densities of the system can now be described by the relations of the solids content by

$$V\phi_\mathrm{s} = N_\mathrm{f}V_\mathrm{f}, \tag{2}$$

where V_f is the volume of the fibres. For fibres with a constant cross-sectional area e.g. non-capped cylindrical fibres, this can be expressed in the form

$$V\phi_\mathrm{s} = N_\mathrm{f}LA_\mathrm{c} = N_s\langle l_\mathrm{s}\rangle A_\mathrm{c}, \tag{3}$$

where L is the length of the fibres, A_c the area of the cross-section of the fibres, and $\langle l_\mathrm{s}\rangle$ is the mean segment length. If the fibres are not allowed to overlap (hard-core case), this solids content ϕ_s is directly related to the apparent density ρ by the relation $\rho = \phi_\mathrm{s}\rho_\mathrm{m}$, where ρ_m is the density of the fibrous (solid) material. Now the relative solids content ϕ_s is given by

$$\phi_\mathrm{s} = \rho_\mathrm{f}LA_\mathrm{c} = \rho_\mathrm{s}\langle l_\mathrm{s}\rangle A_\mathrm{c}. \tag{4}$$

This kind of scaled density is not directly suitable for soft-core networks, as it is not restricted and can have values larger than unity. It has however an interesting meaning in two dimensions i.e. by substituting the volumetric properties of the fibres with the projected areal properties. This kind of density is more commonly known as coverage

$$\rho_\mathrm{A} = \rho_\mathrm{f}A_f, \tag{5}$$

where A_f is the projected area of the fibre.

In some cases it is natural to express the contacts of a single fibre. This is expressed by the coordination number C of the fibre, which is the number of its connected neighbours. The mean of this quantity can be expressed in the form

$$\langle C\rangle = 2\frac{\rho_\mathrm{c}}{\rho_\mathrm{f}}, \tag{6}$$

where the pre-factor 2 takes care of the double-counting of the contacts, as a single contact contributes to the coordination number of both fibres in contact.

2.1.1 Contacts in uncorrelated networks

The assumption of an uncorrelated process leads to a simple way of solving the contact formation. Consider the case of (randomly) adding the last fibre in a test volume V. As each other fibre was added randomly, the expected value of contacts this fibre forms is given by $\langle P_{\text{contact}} \rangle \, (N_\text{f} - 1)$, where N_f is the total number of fibres in the system. The problem then lies in properly determining the probability P_{contact} that two randomly selected fibres will cross. This probability is given by the excluded volume.

The excluded volume of two particles i and j can be defined as 'the volume which is denied to particle j by the condition that it must not intersect particle i' (Onsager, 1949). This volume depends on the geometry of the particles and the relative orientation θ_{ij} between them and can thus be expressed in the form $V_{\text{ex}}(\theta_{ij})$. In 3D we can define that θ_{ij} is taken in the plane parallel to both fibres. Examples of the excluded volume for common elongated objects of equal length are shown in Table 1, but for a more comprehensive list, general solutions are given by Onsager (1949).

Now conveniently, if our test fibre i would be placed randomly into a volume V, where the first fibre j already was placed, the probability of making a contact is $V_{\text{ex}}(\theta_{ij})/V$. For a system of N_f fibres, fibre i will have a total number of $(N_\text{f} - 1)$ such random pairs, and thus the mean coordination number $\langle C \rangle$ is given by

$$\langle C \rangle = (N_\text{f} - 1) \, \frac{\langle V_{\text{ex}}(\theta_{ij}) \rangle}{V}, \tag{7}$$

where the brackets $\langle \cdot \rangle$ denote the expected value of the given quantity. In the special case of an isotropic orientation distribution, this expression can be evaluated directly from the orientation distribution as θ_{ij} can be fixed with respect to an arbitrary vector.

As an example, let us consider a deposited network of N_f rectangles in an area A, of length L and width W. Taking the excluded volume of a rectangle (table 1) and taking the limit $W \to 0$, we find that

$$\langle C \rangle = (N_\text{f} - 1) \, \frac{L^2 \langle \sin\theta \rangle}{A}. \tag{8}$$

Now taking the average of $\sin\theta$ over a uniform distribution we find the result of Kallmes and Corte (1960),

$$\langle C \rangle = \frac{2L^2}{\pi} \frac{N_\text{f} - 1}{A}. \tag{9}$$

This approach is valid for any geometrical shape in both 2D and 3D when the excluded volume and the orientation distribution is known.

Even though the interpretation of the solids content for a soft-core network is a bit ambiguous[3], for a large enough system ($N_\text{f} \gg 1$), it can be useful to express the

[3] For example its relation to apparent density, see (Toll, 1998).

TABLE 1 The excluded volume of some geometric shapes commonly used to describe fibres in 2D and 3D (Balberg et al., 1984; Onsager, 1949). Here θ represents the mean angular difference in the orientation of the objects $\langle\theta_{ij}\rangle$.

Geometry	Excluded volume
2D rectangle	$(L\sin\theta + W + W\cos\theta)(L + W\sin\theta + L\cos\theta) - (L^2 - W^2)\sin\theta\cos\theta$
2D capsule	$4WL + \pi W^2 + L^2\sin\theta$
3D capsule	$(4\pi/3)W^3 + \pi W^2 L + 2WL^2\sin\theta$

behaviour as a function of solids content rather than the number of fibres, and a substitution of N_f in eqn (7) using eqn (2), or equivalently eqn (5) in 2D, leads to

$$\langle C\rangle = \phi_\mathrm{s}\frac{\langle V_\mathrm{ex}\rangle}{V_\mathrm{f}} = \rho_\mathrm{A}\frac{\langle A_\mathrm{ex}\rangle}{A_\mathrm{f}}. \tag{10}$$

2.1.2 Distributional properties

Distributional network properties are important in random networks, as they are the ingredients which make the networks inhomogeneous. There are many aspects for which these properties are important, and they can be observed in many different measurements. Flow properties depend on the local void space (e.g. Publication VI), strength depends on the distribution of contacts (Page, 1969; Carlsson and Lindstrom, 2005) and the mode of deformation depends on the distribution of segments (Heussinger and Frey, 2006; Heussinger et al., 2007).

If the fibre positions and orientations are thought to be drawn independently from some underlying distribution, the contacts can considered to be formed by successive Bernoulli trials with probability p. The probability of getting k successes in n trials is given by the binomial distribution

$$P(X = k) = \binom{n}{k} p^k (1-p)^{n-k}. \tag{11}$$

In such cases $n = N_\mathrm{f}$ is very large and $p = \langle V_\mathrm{ex}\rangle / V$ is very small (and the expected value $np = \langle C\rangle$ is moderate), and the binomial distribution can be approximated by the Poisson distribution,

$$P(X = k) = \frac{\langle C\rangle^k \mathrm{e}^{-\langle C\rangle}}{k!}, \tag{12}$$

where the expected value of X is the mean coordination number $\langle C\rangle$.

Now consider a Poisson point process along a fibre. For a fixed interval at length x, and the mean number of crossings per unit length μ, the probability of finding k crossings in that interval is given by (Deng, 1994)

$$P(X = k) = \frac{(\mu x)^k}{k!}\mathrm{e}^{-\mu x};\ k = 0, 1, 2, \ldots . \tag{13}$$

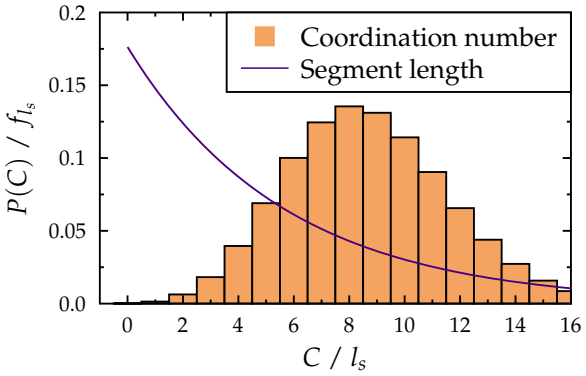

FIGURE 2 Regardless of the exact procedure of network formation, Poisson statistics is an inevitable consequence if hard-core interactions are not accounted for and thus, a negative-exponential distribution of segment length if contacts are evenly distributed along the fibre centreline.

Starting at the end of the fibre, let the first contact on that fibre be at distance x_1. The probability that $x_1 > x$ is then given by

$$P(x_1 > x) = \mathrm{e}^{-\mu x};\ x > 0, \tag{14}$$

from which the complement gives the cumulative distribution function (CDF) of the process, giving us a PDF for the segment length in the form

$$P(l_\mathrm{s} \in [x, x + \mathrm{d}x]) = \mu \mathrm{e}^{-\mu x} \mathrm{d}x,\ x > 0. \tag{15}$$

An example of the resulting distributions in eqs (13) and (15) is shown in fig 2. These statistical properties are to some extent independent of the dimensionality of the network. For $P(C)$ we only need that the contact formation is described by a common random process with a mean probability p. For the segment length distribution it is sufficient that the fibres can be described by a 1D (straight) centreline onto which this Poisson point process can be mapped. This is a very useful result, as any deviation from these distributions, as seen e.g. in the works of He et al. (2004); Blouwolff and Fraden (2006) and Wouterse et al. (2009), can be directly interpreted such that some correlation must exist.

2.2 Voids properties

Equally important as the structure of the network is the structure of the complement i.e. that of the void space. Transport properties, such as fluid flow, show a very different behaviour for different random structures with the same mean properties depending on the details of the structure of the void space (Publication VI).

In the case of networks of infinite lines, the 'pores' of the structure are well defined as the space of $\mathbb{R}^2$ is divided into disjoint polygons. This problem was first addressed by Goudsmit (1945) and further developed by Miles (1964), who derived the distribution of sides in a random polygon, and noted that the average polygon constructed is a rectangle. A common way to approximate this areal distribution is to consider the area of a rectangle, that is constructed by two sides drawn from the negative exponential distribution. The result of the PDF for the area of such a random rectangle is often credited to Corte and Lloyd (1965), but is actually found in the results of Goudsmit (1945). The effect of finite width, i.e. networks of staples, has been considered by Miles (1964) and later by Eichhorn and Sampson (2005).

In 3D the concept of 'pores' is ill-defined. Whereas in 2D, random lines provide an unambiguous tessellation of the space, the corresponding process of placing lines (or cylinders) in $\mathbb{R}^3$ does not. It is thus not surprising that there does not seem to be a consensus of the treatment of 'pores' in 3D. Still some results are given for both distributional (Pan, 1994) and mean values (Neckář and Ibrahim, 2003). One thing that seems to be agreed upon is that the local heights of the void space follow very closely a negative exponential distribution (Hellen and Alava, 1997; Dodson, 2000).

2.3 Effective properties of random networks

Fibrous materials belong to a class of heterogeneous materials i.e. they consist of mixtures of several material components, such as e.g. two different solids (composites), solids and fluids (fibrous networks, solid foams), or fluid mixtures (liquid foams, emulsions), to name a few (Torquato, 2001). It is often beneficial to characterise these materials on a larger macroscopic scale.

On a larger scale, where microscopic details are much smaller than the typical sample size, the macroscopic behaviour of the material can be described by its average, or effective, properties (Torquato, 2001). We shortly introduce here two of these effective properties related to random fibrous structures, viz.: the elastic stiffness tensor $\boldsymbol{C}_{\text{eff}}$ and the fluid permeability tensor $\boldsymbol{k}$.

2.3.1 Elasticity

Elasticity relates to the ability of the medium to withstand external forces applied to the structure. A linear elasticity in continuous media is described by the generalised Hooke's law [e.g. (Saada, 2009)],

$$\boldsymbol{\sigma} = -\boldsymbol{C}\boldsymbol{\epsilon}, \tag{16}$$

where $\boldsymbol{\sigma}$ and $\boldsymbol{\epsilon}$ are the second order stress and strain tensors respectively and $\boldsymbol{C}$ is a fourth-order stiffness tensor. For small deformations the strain tensor can be expressed in the form

$$\epsilon_{ik} = \frac{1}{2}\left(\frac{\partial u_i}{\partial x_k} + \frac{\partial u_k}{\partial x_i}\right). \tag{17}$$

The coefficients of the strain tensor C_{ijkl} can be reduced by the symmetries of the stress tensor $C_{ijkl} = C_{jikl}$, symmetries of the strain tensor $C_{ijkl} = C_{ijlk}$ and symmetries induced by existence of the strain density function, $C_{ijkl} = C_{klij}$. As a result, we have 21 independent coefficients describing the stiffness tensor C.

Further assumptions of symmetry reduce the number of independent coefficients. In the special case of an isotropic medium, they are reduced to just two, and eqn (16) can be expressed in the form

$$\sigma_{ij} = 2\mu\epsilon_{ij} + \lambda\delta_{ij}\epsilon_{nn}, \tag{18}$$

where μ and λ are the Lamé parameters. Lamé parameter λ is more commonly known as the shear modulus. With these parameters we can also express the more commonly used Young's modulus $Y = \frac{\mu(3\lambda+2\mu)}{\lambda+\mu}$ and Poisson ratio $\nu = \frac{\lambda}{2(\lambda+\mu)}$, where Y relates directly to the one dimensional extension/compression of the material, whereas the Poisson ratio ν relates to the transverse strain transfer.

The first mean field theory of elasticity of fibre networks was developed by Cox (1952), who derived the 21 coefficients of the stiffness tensor C of a random line network consisting of non-interactive fibres that span the whole sample volume (both 2D and 3D). The special case of 2D furthermore assumed that this bending stiffness is negligible so that the elastic coefficients are now given by

$$\begin{aligned} Y_{\text{eff}} &= \frac{1}{3}\rho_{\text{f}} Y A_{\text{c}} \\ G_{\text{eff}} &= \frac{1}{8}\rho_{\text{f}} Y A_{\text{c}} \\ \nu &= \frac{1}{3}, \end{aligned} \tag{19}$$

where Y_{eff} and G_{eff} are the effective Young's and shear modulus of the network respectively and Y is the Young's modulus of the fibres.

The rise of paper science saw many models being developed during the 60s and 70s (see e.g. Baum (1984) for a survey). Cox also introduced the concept of stress transfer from the surrounding matrix to the fibre which was extended by Page et al. (1979) in their shear lag model by considering fibres of a finite length, so that this stress transfer happened via contacts in the fibre network. Such a correction deviated from that of the infinite line networks such that

$$Y = \frac{1}{3} Y A_{\text{c}} \left(\rho_{\text{f}} - K\rho_{\text{fc}}\right), \tag{20}$$

where ρ_{fc} is the fibre density at a stiffness percolation of the random network and K is a constant related to the rate of stress transfer to the fibres. This correctly

predicted a stiffness percolation of the network i.e. there exists a percolation density in which the network starts to store elastic energy globally (Latva-Kokko et al., 2001; Latva-Kokko and Timonen, 2001; Heussinger and Frey, 2006). The concept of shear lag has also been considered in fracture mechanics (Carlsson and Lindstrom, 2005).

Further work on the stiffness of random networks has been done by taking the affine displacement field of Cox (1952), but considering the behaviour of single segments, modelled by either Euler-Bernoulli beams (Åström et al., 2000a,b) or Timoshenko beams (Wang and Sastry, 2000; Wu and Dzenis, 2005; Berhan and Sastry, 2007). A notable requirement of these models is the full knowledge of the PDF for the segment lengths f_{l_s}.

Numerical studies on the elasticity of random networks have also revealed an intermediate region (Wilhelm and Frey, 2003; Heussinger et al., 2007; Head et al., 2003; Buxton and Clarke, 2007), where the elastic response is highly non-affine. This relates to the deformation being governed by segment bending rather than stretching (Heussinger and Frey, 2006; Heussinger et al., 2007) of the fibres. Similar behaviour has also been observed on bond-diluted lattice based systems (Broedersz et al., 2011, 2012). All these models, except for the noninteracting case of (Cox, 1952), require detailed information of the connectivity. Moreover, the affine to non-affine crossover can be directly linked to the segment lengths of the network.

2.3.2 Permeability

At low Reynolds numbers, in the limit of Stokes flow, fluid flow through a porous medium is well described by Darcy's law (Bear, 2013),

$$\boldsymbol{q} = -\frac{\boldsymbol{k}}{\mu}\boldsymbol{\nabla} p, \tag{21}$$

where $\boldsymbol{q}$ is the flow velocity, μ the dynamic viscosity of the fluid and $\boldsymbol{\nabla} p$ the fluid pressure gradient. Permeability coefficient $\boldsymbol{k}$, a second rank tensor, measures the conductivity to fluid flow of the porous material and is usually a priori unknown.

The most widely used phenomenological expression which relates permeability to structural characteristics of the porous material is the Kozeny-Carman law (Kozeny, 1927; Carman, 1937),

$$k = \frac{\phi^3}{CS^2}, \tag{22}$$

where $\phi = (1 - \phi_s)$ is the porosity and S is the relative surface of the sample. C is the Kozeny coefficient, which is a material dependent constant and includes the effect of tortuous flow paths in the medium. Another form of the equation, which is also common in the literature, is given by

$$k = \frac{1}{cS_0^2}\frac{\phi^3}{\tau^2\left(1-\phi\right)^2}, \tag{23}$$

where $S_0 = S/\phi_s$ is the specific surface area i.e. normalised by the solids content, τ is the tortuosity, and c is now the Kozeny-Carman constant.

Although many models have been proposed for the flow in porous materials (Jackson and James, 1986; Nilsson and Stenström, 1997; Higdon and Ford, 1996; Tomadakis and Robertson, 2005; Soltani et al., 2014) there seems not to be a consensus on how flow behaves in them. Numerical works on the subject include e.g. uncorrelated soft core networks (Nabovati et al., 2009), deposited networks (Koponen et al., 1998) and randomly grown hard core networks (Stylianopoulos et al., 2008), which each have lead to a different empirical treatment of the subject respectively.

The flow can also be related to the pore structure of the void space, where the fluid actually flows. This idea dates back to Purcell (1949), who considered flow systems of parallel capillaries with varying radii, and has also been extended to include the effect of connectivity (Childs and Collis-George, 1950; Scheidegger, 1957; Marshall, 1958). Very recently Huang et al. (2015) linked the permeability of fibrous structures with their local void sizes. In Publication VI we derive a generalisation of the Kozeny-Carman model for fluid flow trough parallel disperse capillary tubes. We notice that, in addition to a mean length scale (which is embedded in the specific surface S_0), the distribution of the void space is an equally important factor in the permeability.

2.4 Steric models

By a steric hindrance we mean the geometric obstruction between fibres so that they cannot overlap in space. This introduces restrictions to the positions and orientations of the fibres, and thus introduces correlations between the constituents of the network.

There are two main methods which have been used to incorporate this in the models of random networks. One approach involves considering the reduction of available configuration space [e.g. (Pan, 1993; Komori and Itoh, 1994)]. The other involves taking the approximation of thin networks (Kallmes and Corte, 1960) and applying the steric hindrace between multiple layers of such networks [e.g. (Kallmes and Corte, 1961; Sampson, 2004; Bagherzadeh et al., 2012)]. For better comparability we report here only results for planar random networks.

The effect of existing rods restricting the possible locations of others was considered by Pan (1993) who described this steric hindrance by reduction in the probability of contacts $P = \frac{V_{ex}}{V}\left(1 - \bar{d}_i\right)$, where $\bar{d}_i$ is the normalised 'forbidden length' owing to pre-existing contacts in the fibre,

$$\rho_c = \frac{32}{W^3\left(\pi^3 + 16A\phi_s\right)}\phi_s^2, \tag{24}$$

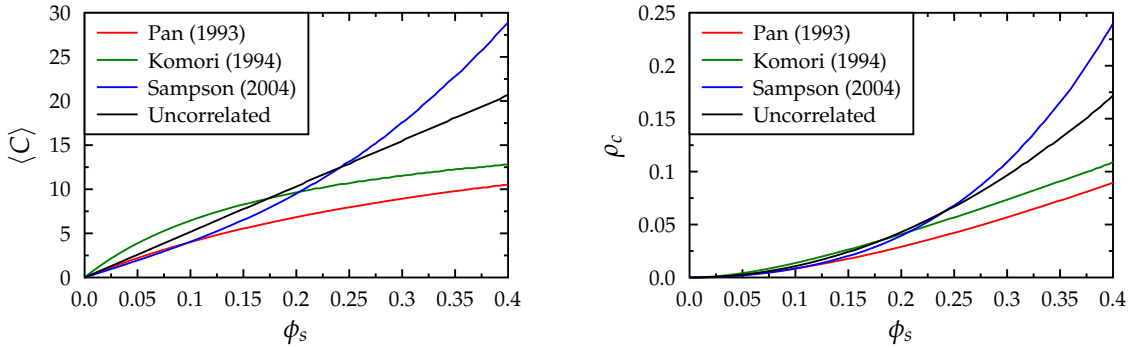

(a) Coordination number (b) Contact density

FIGURE 3 Comparison of different models for the coordination number $\langle C \rangle$ (a) and contact density ρ_c (b) for a random network with $L/W = 30$. The number of levels in the model of Sampson (2004) was chosen arbitrarily as 10.

where $A = \log\{\cot[\arcsin(W/L)]\}$ is a constant only depending on the aspect ratio of the fibre. This result was extended by Komori and Itoh (1994) who, by correcting some mathematical and logical shortcomings, found that

$$\rho_c = \frac{32}{\pi^3 W^3} h \phi_s^2, \tag{25}$$

where $h = 2/(1 + 16\pi\phi_s)$.

The effect of multiplanar steric hindrance was already considered by Kallmes and Corte (1961) and Kallmes and Bernier (1962) addressing both the number of contacts and correspondingly the relative bonding of the networks. The basic principle was to consider stacks of thin networks (networks with a small coverage) and account for the interlayer contacts separately. These kinds of models have been extended later by e.g. Sampson (2004) and Bagherzadeh et al. (2012). Sampson (2004) derives the contact number such that $\langle C \rangle = 2(LW/A)\Phi^*_{\mathrm{mp}}$, where A is the expected area of a contact, and

$$\Phi^*_{\mathrm{mp}} = \frac{1}{n}\left[(n-2)\left(\Phi^{2\mathrm{D}} + \Phi^*\right) + \Phi^*\right], \tag{26}$$

where $\Phi^{2\mathrm{D}}$ and Φ^* are respectively the relative contact area of thin networks and interlayer contacts. In fig. 3 we plot the different models of steric hindrance and compare them with results for the corresponding uncorrelated network of capsules. It is evident, that the models differ substantially from each other and do not even agree on the general shape of the function $\langle C \rangle(\phi_s)$.

A different field, in which steric hindrance is important is in the thermodynamical treatment of hard rods (Onsager, 1949; Lekkerkerker et al., 1984). This connection has indeed been done by e.g. Philipse (1996) who noted that the random packing of hard rods produce dense isotropic networks. So dense, that the metastable systems are only stable in a macroscopic limit, as colloidal fluids would spontaneously seek a nematic order at similar density. Indeed, albeit the

many analytically solved properties of these systems, their usefulness for solving properties of macroscopic packed systems seem to be limited. To the author's knowledge contact formation in these kinds of statistical many-body systems are zero-probability events, i.e. configurations that result of contacts between particles belong to a zero-measure manifold of the allowed configuration space and contacts would have to be defined by some arbitrary soft-core extension. Moreover, deposited system tend to form planarly packed networks, a state that is not present in the phase diagram for colloidal systems (Bolhuis and Frenkel, 1997; Dijkstra et al., 2001). A rigorous treatment of these models is beyond the scope of this Thesis and is not discussed here.

3 TOMOGRAPHY

The word Tomography (from the greek words *tomos* and *graphō*) simply means the method of slice imaging. That is, the obtaining of a 3D image by combining slices of 2D images from within the sample. X-ray tomography refers to the (non-destructive) method of obtaining 3D images by reconstruction of radiographs of the sample. Around the millennial shift the resolution of commercial desktop scanners got into the μm scale and micro scale computed tomography (μCT) saw a rise of popularity in materials science becoming a significant tool for structural imaging (Stock, 1999; Maire et al., 2001; Salvo et al., 2003).

Although the mathematical tools and proof for the tomographic reconstruction based on radiography were developed as early as 1917 by Radon, practical applications came much later. The first reported commercial devices were developed during to 70s by Hounsfield. The development of the resolution of these kinds of devices has allowed for utilization of μCT also in materials science including fibrous materials such as metallic foams (Elliott et al., 2002; Maire et al., 2003; Blacher et al., 2004; Montanini, 2005; Dillard et al., 2005), composite materials (Lux et al., 2006; Miettinen et al., 2012) and granular piles (Seidler et al., 2000; Richard et al., 2003; Moreno-Atanasio et al., 2010) only to name a few.

The tomographic imaging used for this work was done with the two μCT devices located in the facilities of the Department of Physics at the University of Jyväskylä, Finland. The paper fibre networks were all imaged using an Xradia Micro-XCT-400 device, while the images of randomly packed spaghetti strands were obtained using a SkyScan 1172 μCT scanner.

3.1 X-ray imaging

In principle, the X-ray imaging used in μCT works in very much the same way as in conventional radiography, the difference being that the either sample or

detector-camera setup is mounted in such a way that projections from different angles can be taken.

In most desktop μCT scanners the beam is generated with a traditional X-ray tube. In a conventional X-ray tube the beam is generated by accelerating a focussed electron beam on an anode (the most widely used material being tungsten). Upon collision with the anode, the electrons deaccelerate and produce both a continuous spectrum of Bremsshtrahlung and characteristic peaks depending on the material of the target.

3.1.1 Interaction with matter

The method of X-ray imaging (be it 2D or 3D) is based on the attenuation of X-rays passing through media, mainly by photoelectric absorption, inelastic Compton scattering and Rayleigh scattering[1]. For a monochromatic beam passing through a homogeneous material of thickness x, the intensity of the attenuated beam follows the Beer-Lambert law

$$I = I_0 \mathrm{e}^{-\mu x}, \tag{27}$$

where I_0 is the intensity of the unattenuated beam and μ is the linear attenuation coefficient. The linear attenuation coefficient μ is the (normalized) sum of the interaction cross-sections of the target material and depends thus strongly on the atomic number Z, and consequently approximately on the density. These interaction probabilities, however, depend strongly also on the energy of the beam. In most desktop scanners (also in our case) the beam has a broad energy spectrum, and the recorded intensity is given by the integration

$$I = \int I_0(E)\, \mathrm{e}^{-\mu(E)x}\, \mathrm{d}E. \tag{28}$$

As many detectors record only absolute intensity, these polychromatic spectra of the beams can cause reconstruction artefacts in the sample, such as e.g. beam hardening, i.e. the increase of mean energy as the beam travels through a sample. This is, however, a difficulty more related to the imaging of denser materials, such as minerals, and the effect on the image quality in our work is negligible.

3.2 Reconstruction

For the sake of simplicity, let us assume a parallel monochromatic beam passing trough a sample, which has a spatial distribution of attenuation described by the function $f : \mathbb{R}^2 \to \mathbb{R}$. We can rewrite eqn (27) in the differential form, i.e., the

[1] Generally the energies used in X-ray imaging are low enough so that the cross-section of pair-production can be ignored.

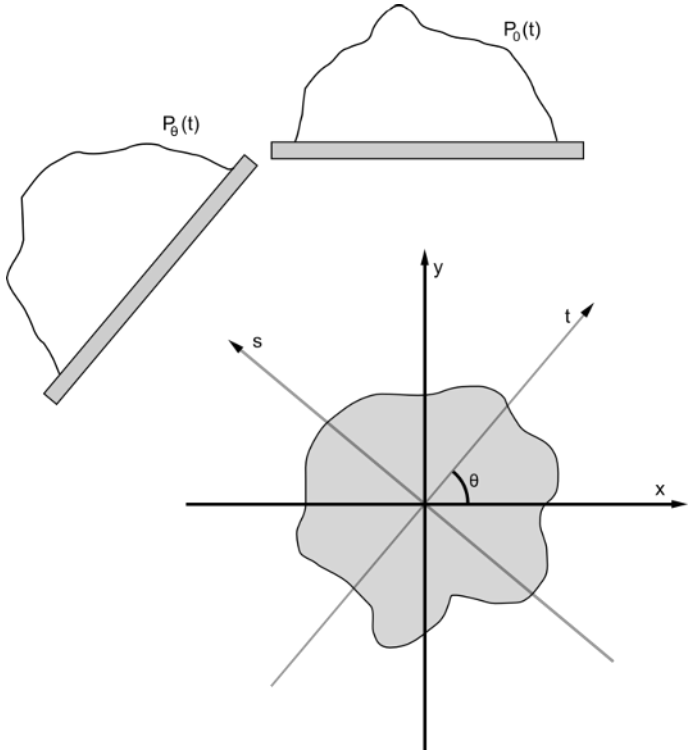

FIGURE 4 A sample described by its local attenuation coefficient $f(x, y)$ and two examples of projection, i.e. its Radon transform $Rf(x, y) = P_\theta(t)$. One at angle 0, $P_0(t)$, and one at angle θ, $P_\theta(t)$.

attenuation that occurs within a small thickness element ds in the sample

$$\frac{\mathrm{d}I}{I} = -\mu \,\mathrm{d}s = -f(x, y)\,\mathrm{d}s. \tag{29}$$

The recorded attenuation in the radiographs are each given by a projection (parallell line integrals) over this attenuation function $f(x, y)$ (see fig. 4). By defining the rotated coordinate system as

$$\begin{bmatrix} t \\ s \end{bmatrix} = \begin{bmatrix} \cos\theta & \sin\theta \\ -\sin\theta & \cos\theta \end{bmatrix} \begin{bmatrix} x \\ y \end{bmatrix}, \tag{30}$$

we can describe these recorded attenuation images for an arbitrary rotation angle θ as

$$P_\theta(t) = \int_{-\infty}^{\infty} f(t, s)\,\mathrm{d}s. \tag{31}$$

This function, mapping the density distribution function $f(x, y)$ to its rotated projections $P_\theta(t)$, is more commonly known as the Radon transform $Rf(\theta, t)$. The existence of the inverse of this function is the mathematical basis for modern μCT imaging.

Consider now the Fourier transform of the projection data for one slice at an

angle of θ, which can be written as

$$S_\theta(\omega) = \int_{-\infty}^{\infty} P_\theta(t) e^{-\mathrm{i}2\pi\omega t}\,\mathrm{d}t. \tag{32}$$

Substituting $P_\theta(t)$ with eqn (31) and transforming it into the (x, y) coordinate system by relation eqn (30) we find that

$$S_\theta(\omega) = \int_{-\infty}^{\infty}\int_{-\infty}^{\infty} f(x,y) e^{-\mathrm{i}2\pi\omega(x\cos\theta + y\sin\theta)}\,\mathrm{d}x\mathrm{d}y, \tag{33}$$

which is conveniently just the two dimensional Fourier transform of a function $f(x, y)$

$$F(u,v) = \int_{-\infty}^{\infty}\int_{-\infty}^{\infty} f(x,y) e^{-\mathrm{i}2\pi(ux+vy)}\,\mathrm{d}x\mathrm{d}y, \tag{34}$$

with the constraints $u = \omega\cos\theta$ and $v = \omega\sin\theta$, which in this case is the line of the projection. So for every Fourier transform of the projection $P_\theta(t)$ we fill the frequency domain at an angle of θ. Consequently, collecting an infinite number of projection data at different angles would result in the complete Fourier transform of the object.

3.2.1 Filtered backprojection

The most commonly used reconstruction methods for tomographic images are based on Filtered Backprojection. As the name suggests, the reconstruction is obtained by backprojecting a modified, 'filtered', projection image onto the reconstruction volume. Although most desktop μCT devices do not have a parallel beam, the underlying idea is very similar and reconstructions can be obtained with slight modifications, see e.g. Feldkamp et al. (1984), Kak and Slaney (1999) and Turbell (2001).

The inverse Fourier transform of $F(u, v)$ in eqn (34) is given by

$$f(x,y) = \int_{-\infty}^{\infty}\int_{-\infty}^{\infty} F(u,v) e^{\mathrm{i}2\pi(ux+vy)}\,\mathrm{d}u\mathrm{d}v. \tag{35}$$

By expressing this in polar coordinates by making the substitution $u = \omega\cos\theta$ and $v = \omega\sin\theta$ in eqn (35) and by substituting the Fourier transform of the projection at angle θ, $S_\theta(\omega)$ for the Fourier transform $F(\omega, \theta)$ one can write the transform as

$$f(x,y) = \int_{0}^{\pi}\int_{-\infty}^{\infty} S_\theta(\omega)|\omega| e^{\mathrm{i}2\pi\omega t}\,\mathrm{d}\omega\mathrm{d}\theta. \tag{36}$$

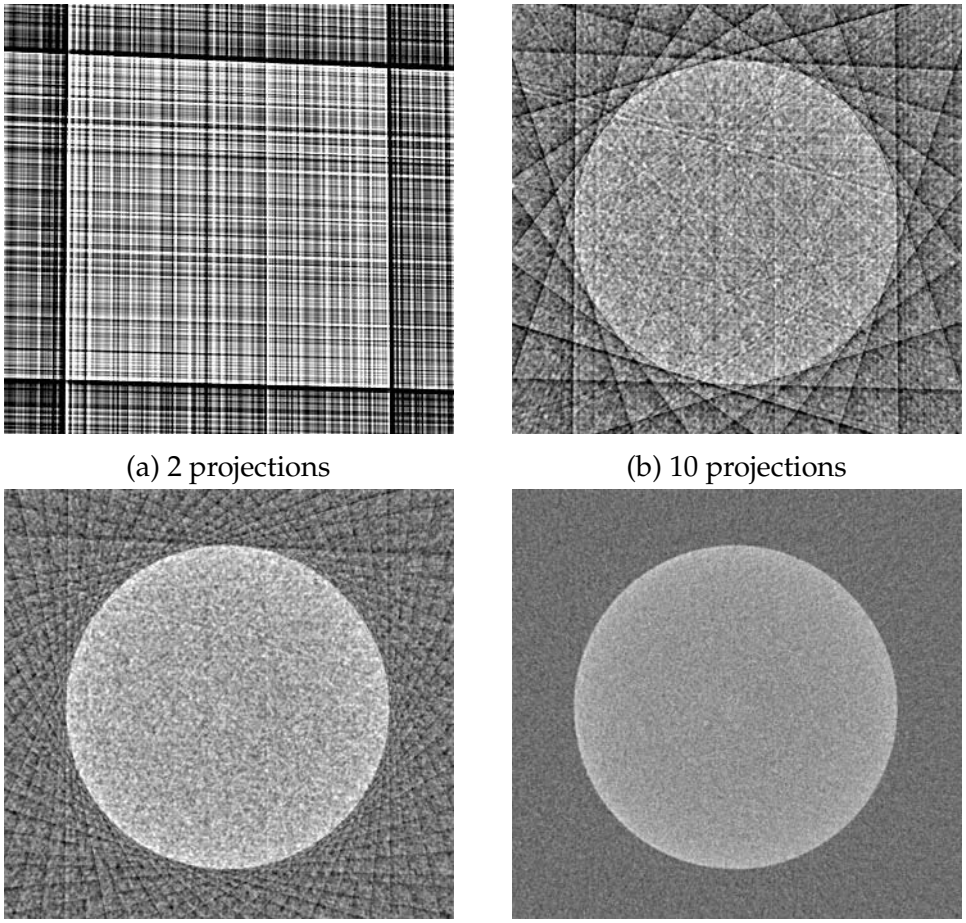

(a) 2 projections (b) 10 projections

(c) 30 projections (d) 181 projections

FIGURE 5 A reconstruction of a spherical object using different number of projections.

By substituting eqn (32) for $S_\theta(\omega)$ and rearranging, we get

$$f(x,y) = \int_0^\pi \int_{-\infty}^{\infty} P_\theta(t') G(t-t') \, \mathrm{d}t' \mathrm{d}\theta, \tag{37}$$

where $G(t-t') = \int |\omega| e^{\mathrm{i}2\pi\omega(t-t')} \, \mathrm{d}\omega$. This is the underlying idea of the filtered backprojection. A filter, G (often called a ramp filter owing to the shape in the Fourier space), is applied on the projections P_θ. The result is 'smeared' or backprojected onto the image as in fig. 5. The reconstructed image consists of contributions of this backprojection from each angle θ.

In practice, the devices recording the data are naturally not continuous and the exposure time sets limits on the amount of projections taken. Owing to this imaging is always a balancing of available time and required quality. In fig. 5 we show an example of a tomographic reconstruction showing the effect of noise (single pixel streaking), the number of projections (increasing detail of the spherical boundary) and beam hardening (edges of the sample appear more dense).

3.3 Image analysis

Although raw reconstructed 3D images as such can be a powerful tool to assess many qualitative questions, they are not always directly suitable for quantitative analysis. Moreover, the methods of extracting relevant data from the images are computationally challenging. Modern μCT devices produce 3D images that are roughly three orders of magnitude larger than corresponding 2D images. This means that not all of the conventional image processing procedures are directly applicable on 3D images. A recent review on 3D image processing, especially for material research, is given by Turpeinen (2015).

3.3.1 Problems

Reconstructions are never without some defects (Stock, 2009). These may be device specific artefacts, owing to improper scanner calibration, or faults in the detector. They can also be sample specific errors caused by streaking of high-density particles or inaccuracies owing to sample sizes larger than the field of view. Moreover, pure statistical fluctuations both relating to the X-ray source, attenuation, and detector cause random noise in the final image. Owing to these effects, images may require a substantial amount of pre-processing before being suitable for analysis.

Samples in our work were assumed homogeneous with respect to their material density. This leads to a general problem in μCT given a gray-scale reconstruction of a sample. How do we define what is considered solid and what is not? In practice this definition is often problem dependent. With e.g. the granular piles of short-cut spaghetti, we conducted a separate measurement of strand thickness, which was then used as a proper criteria. In other samples, where it was imperative that the voids of the sample did not contain single floating solids voxels, an stricter threshold for solids was justified.

3.3.2 Mehtods

Although the focus of this Thesis is not on image processing, for clarity, we introduce two image processing methods, as they were used in the studies.

Distance transforms (Borgefors, 1986) are operators on foreground voxels which gives the shortest (local) distance to a chosen object. The distance here is defined such that paths only travel along these foreground voxels. In our method (see section 4) the shortest transverse path along fibre networks was done by applying a distance transform on the solids voxels of the image using the solids voxels in an xy-plane as the object. At that time, no fast implementation of Euclidian distance transforms was available and thus the results were acquired by Chamfer masking (Barrow et al., 1977; Remy and E, 2000).

The local thickness (Hildebrand and Rüegsegger, 1997) is a local measure of the void space which gives, for each point (x, y, z), the diameter of the largest sphere that fits inside the void space containing the point (x, y, z). In our work we used the implementation by Dougherty and Kunzelmann (2007).

4 THE EFFECT OF STERIC HINDRANCE ON THE STRUCTURE OF NETWORKS

Although it is evident that realistic fibre networks do include steric effects in their packing, as e.g. piles of spaghetti do not collapse into each other, the actual quantifiable evidence of the effect is very sparse for elongated objects. Direct measurements on networks and piles (He et al., 2004; Blouwolff and Fraden, 2006; Marulier et al., 2012) reveal characteristics in their distributions that, in hindsight, are clear indications of this effect, but have gone unnoticed.

The effect of the steric hindrance has often been neglected with the argument that it should vanish at a large aspect ratio. This is partially true and well supported by heuristic arguments (Toll, 1998) for global properties and by correct predictions of uncorrelated models. For example in 3D the random packing of stiff constituents is governed by their geometry. Famously, the random packing of identical spheres reaches a random close packing[1] of $\phi_s \approx 0.64$ with a mean coordination number of $\langle C \rangle = 6$. For prolate particles, this random packing fraction ϕ_s approaches 0 as the aspect ratio increases. This was related to random uncorrelated networks by Philipse (1996), who argued that for a random collection of rods, where

$$2\phi_s \frac{L}{W} = \langle C \rangle, \tag{38}$$

$\langle C \rangle$ is restricted by requirements of global rigidity, i.e., a certain number of contacts is required (regardless of the aspect ratio) for mechanical stability of the pile. This agrees remarkably well with experimental results for rods of large aspect ratio with a mean coordination number $\langle C \rangle = 10.8$ and both numerical and experimental studies show similar results (Williams and Philipse, 2003; Blouwolff and Fraden, 2006; Wouterse et al., 2009). The effect of steric hindrance on statistical properties have, however, remained elusive.

[1] The term 'random close packing' has been criticised by Torquato et al. (2000), where they introduce the concept of 'maximally random jammed state', which in contrast to RCP is a well defined criterion corresponding to the least ordered of all jammed states.

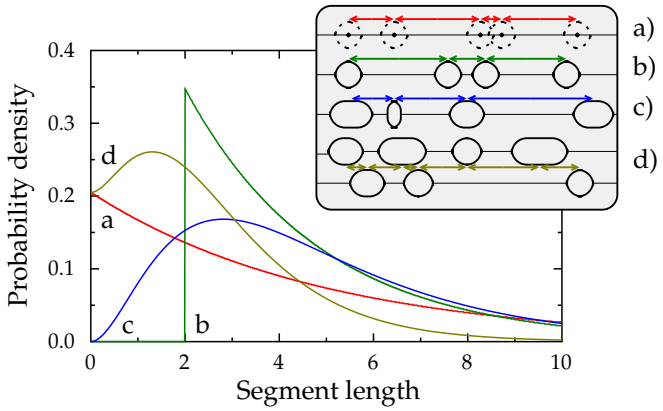

FIGURE 6 Schematic representation of different contact formation processes, viz.: A Poisson process (a), a homogeneous Tonks gas (or equivalently a Gibbs point process) (b), a disperse Tonks gas (c) and two superposed disperse Tonks gases (d).

In this chapter we introduce our model for the sterically hindered contact formation and extend it to a geometrical model of random fibre networks with applications for measurement methods for real materials.

4.1 Steric model for contact formation

In order to understand how the steric hindrance affects contact formation we reduced the complexity of the problem as much as possible, i.e. to a 1D point process. We base our model on the approximation that the contacts on a fibre can be divided so that they are either on its top or bottom side. This is justified if the system meets two criteria. Firstly, the starting configuration needs to be dilute enough, so fibres can be classified in an ordered set of deposition, this is trivially met if the fibres are deposited one by one. Secondly, the friction must be high enough, so sliding and rearrangement during the deposition does not alter this order.

These two uncorrelated contact forming processes are modelled as separate hard-core systems. If neighbouring fibres on one side would always cross in right angles, this process would be sterically hindered such that $P(l_s < w_f) = 0$. A system that follows this steric hindrance, but is otherwise random, is the Tonks gas of hard spheres (Tonks, 1936) (fig. 6b).

We extend the result by Tonks (1936) extending this linear gas to particles of an arbitrary size distribution (fig. 6c). Finally, the proposed model for a sterically hindered contact formation proces is given by superposition of the two separate hard-core systems (fig. 6d).

4.1.1 Tonks gas of disperse particles

Tonks gas is a system of uniform particles with hard core repulsions confined into a one dimensional space. Here we repeat the statistical analysis of the system, following Tonks (1936), but extend it to arbitrary particle size distributions.

Let X_i be the (random variables of) point positions of N particles, each with a separate diameter d_i confined in a linear space of length L. We denote in addition the (continuous) positions of the particles by general coordinates x_i. Without loss of generality, we can number the particles according to their positional order. Ordering of the particles gives rise to restrictions for the possible particle positions x_i. Here we use the same restrictions as Tonks (1936), but with individual d_i for each particle, such that

$$\begin{aligned} x_1 &> x_1^{\min} = d_1/2 \\ x_i &> x_i^{\min} = \sum_{k=1}^{i-1} d_k + d_i/2, \text{ for } i > 1 \\ x_i &< x_i^{\max} = x_{i+1} - (d_{i+1} + d_i)/2 \text{ for } i < N \\ x_N &< x_N^{\max} = L - d_N/2. \end{aligned} \tag{39}$$

The total volume of the configuration space of the system M_N can now be found by integrating over all possible point positions constrained with the hard-core interactions,

$$M_N = \int_{x_N^{\min}}^{x_N^{\max}} \dots \int_{x_2^{\min}}^{x_2^{\max}} \int_{x_1^{\min}}^{x_1^{\max}} \mathrm{d}x_1 \mathrm{d}x_2 \dots \mathrm{d}x_N, \tag{40}$$

and we find further that M_N is now given by

$$M_N = (L - N\langle d \rangle)^N / N!, \tag{41}$$

where $\langle d \rangle$ is the average over d_i. The density of states $M_{N-1}(x_N)$ relative to x_N can be found, exactly as in (Tonks, 1936), by skipping integration over the last variable, such that

$$\begin{aligned} M_{N-1}(x_N) &= \int_{x_{N-1}^{\min}}^{x_{N-1}^{\max}} \dots \int_{x_2^{\min}}^{x_2^{\max}} \int_{x_1^{\min}}^{x_1^{\max}} \mathrm{d}x_1 \mathrm{d}x_2 \dots \mathrm{d}x_{N-1} \\ &= \frac{\left(x_N - d_N/2 - \Sigma_1^{N-1} d_i\right)^{N-1}}{(N-1)!}. \end{aligned} \tag{42}$$

The probability density function (PDF) of the point position X_N is then found by normalising, and we find that

$$\begin{aligned} f_{X_N}(x_N) &= M_{N-1}/M_N \\ &= N \frac{\left(x_N - d_N/2 - \Sigma_1^{N-1} d_i\right)^{N-1}}{(L - N\langle d \rangle)^N}. \end{aligned} \tag{43}$$

Following further the derivation by Tonks (1936), we suppose that the boundary is a fixed particle with its centre at $L + d_L/2$, and thus the segment length l_s between the last particle and the boundary can be expressed by a variable

$$x = L + d_L/2 - x_N, \tag{44}$$

and we find that the probability density function for segment lengths is given by

$$f_{X_L}(x) = \frac{N}{L - N\langle d\rangle}\left[1 - \frac{x - (d_L + d_N)/2}{L - N\langle d\rangle}\right]^{N-1}, \tag{45}$$

which in the limit of large L, i.e. $L \gg \langle d\rangle$, becomes

$$f_\mu(x) = \mu \exp\left[-\mu\left(x - \frac{d_L + d_N}{2}\right)\right]; x \geq \tfrac{d_L+d_N}{2}, \tag{46}$$

in which $\mu := \langle C\rangle/(L - \langle C\rangle\langle d\rangle)$. Assuming that particle sizes are independent, but drawn from the same distribution, we can derive a single PDF for the steric hindrance between the two adjacent particles. By denoting $d_{12} := \frac{d_l+d_N}{2}$ and by the convolution $f_{d_{12}} = (f_{d/2} \otimes f_{d/2})$, where

$$P(d/2 \in [x, x + \mathrm{d}x]) = f_{d/2}(x)\,\mathrm{d}x, \tag{47}$$

we find that

$$P(l_s \in [x, x + \mathrm{d}x], d_{12} \in [y, y + \mathrm{d}y]) = f_{d_{12}}(y)\mu \mathrm{e}^{-\mu(x-y)}\,\mathrm{d}x\mathrm{d}y; x \geq y. \tag{48}$$

Distribution of segment lengths is finally given by the marginal distribution,

$$f_{l_s}(x) = \int_0^x f_{d_{12}}(y)\mu \mathrm{e}^{-\mu(x-y)}\,\mathrm{d}y. \tag{49}$$

Notice that here integration extends only to $y = x$, as $f_\mu(x)$ is only supported by positive values of $(x - y)$ and eqn (49) is simply a convolution of a distribution of steric hindrances, $f_{d_{12}}$, and a negative exponential distribution f_μ, with a process frequency of μ, i.e.

$$P(l_{s1} \in [x, x + \mathrm{d}x]) = \mathrm{d}x\left(f_{d_{12}} \otimes f_\mu\right). \tag{50}$$

This means that segment length can be thought of as a combination of two uncorrelated elements: An inter-particle distance from a Poisson point process in a reduced configuration space, and a steric hindrance induced by two adjacent particles.

4.1.2 Superposition of uncorrelated processes

For identical particles, the Tonks gas can be thought of as a renewal process with inter-event times l_{s1} given by a random process with the PDF f_{l_s}. With this analogy,

the segment lengths of p superposed processes is readily given by Lawrence (1973),

$$1 - F_{\mathrm{p}}(x) = [1 - F_1(x)] \left[c \int_x^\infty 1 - F_1(s)\, \mathrm{d}s \right]^{p-1}, \tag{51}$$

in which $F_1(x)$ is the cumulative distribution function (CDF) of segment lengths of the Tonks gas, and $c = \langle C \rangle / L$ is the contact density in 1D (along a fibre). The cumulative distribution of a shifted exponential distribution is given by

$$F_1(x) = \begin{cases} 0 & ; x \leq d, \\ 1 - \mathrm{e}^{-\mu(x-d)} & ; x > d. \end{cases} \tag{52}$$

Combining eqns (51) and (52) we find that the superposed CDF of two-sided contacts between particles, i.e. for contacts on the both top and bottom sides of them, is given by

$$F_2(x) = \begin{cases} 1 - \left[\mu^{-1} + (d - x)\right] c & ; x \leq d, \\ 1 - \frac{c}{\mu} \mathrm{e}^{-2\mu(x-d)} & ; x > d. \end{cases} \tag{53}$$

For $c = \frac{\langle C \rangle}{L}$ and $\mu = \frac{\langle C \rangle}{L - \langle C \rangle d}$ eqn (53) is continuous at d, $F_2(0) = 0$ as expected, and the distribution of segment lengths for two combined processes is given by

$$f_{l_{\mathrm{s}},2}(x) = \frac{d}{dx} F_2(x) = \begin{cases} c & ; x \leq d, \\ 2c\mathrm{e}^{-2\mu(x-d)} & ; x > d. \end{cases} \tag{54}$$

For the superposition of the Tonks gas of non-identical particles, we have to make a slight approximation as the renewal process requires independent intervals. As is evident from fig. 7, modelling the gas with particles of non-zero size d_i is now not suitable as the segment lengths on both sides of that particle X_i depend on the same particle size, d_i, and are thus correlated. We thus have to assume, as for the one-sided segment lengths, that the steric hindrances between neighbouring particles are independent i.e. can be drawn from a distribution $f_{d_{12}}(x)$.

With this assumption the segment lengths of the superposed process can be determined from eqn (51) with CDF in the form

$$F_1 = \int_0^x f_{l_{\mathrm{s}}}(t)\, \mathrm{d}t = \int_0^x \int_0^t f_{d_{12}}(y) \mu \mathrm{e}^{-\mu(t-y)}\, \mathrm{d}y \mathrm{d}t. \tag{55}$$

Denoting here $h(x) = [1 - F_1(x)]$ and $g(x) = \int_x^\infty [1 - F_1(s)]\, \mathrm{d}s$ the segment length distribution $f_{l_{\mathrm{s}},p}$ for p superposed processes is finally given by

$$f_{l_{\mathrm{s}},p}(x) = c^{p-1} \left[f_{l_{\mathrm{s}},1}(x) g(x)^{p-1} + (p-1) h(x)^2 g(x)^{p-2} \right]. \tag{56}$$

Because particle centres in a disperse Tonks gas cannot be described by a renewal process, we described the steric hindrance as a property between two neighbouring particles instead. So as to test whether this approximation has any effect on

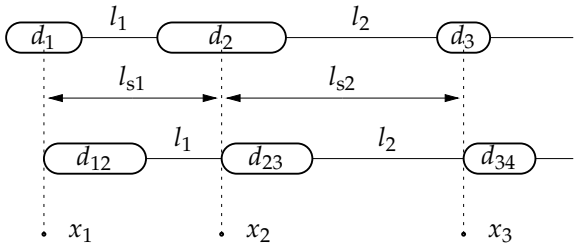

FIGURE 7 A system of disperse particles with centres x_i cannot (strictly speaking) be modelled as a renewal process. Segment lengths l_{s1} and l_{s2} shown here are correlated as they depend on the same particle size d_2. To circumvent this problem, we approximatively consider the steric hindrance as an uncorrelated effect between two neighbouring particles d_{ij}. This approximation has, however, no effect on the segment length distribution.

the derived distribution of segment lengths, simulated realisations of the Tonks gas were done with particle sizes drawn from a negative-exponential distribution ('true' solution). This was done by sampling a 1D Poisson process in a configuration space with a reduced length $L - C\langle d \rangle$, and 'inflating' the zero-measure points of the Poisson process to a finite size d_i drawn from a negative-exponential distribution. As for the one-sided process, where the segment length distribution is identical regardless of whether the steric hindrance is described as a property of one particle or particle pairs, the approximation of independent steric hindrances induced by particle pairs has no effect on the segment length distribution.

4.1.3 Choice of particle size distribution

The final part of our sterically hindered theory for the contacts is the actual distribution of steric hindrance $f_{d_{12}}$ for which we have no obvious candidate. One possibility is to incorporate the angular distributions of the fibres similar to (Kantor and Kardar, 2009), who considered a linear gas of randomly aligned needles, but as our fibres are flexible, the proper effective length of our needles may be both disperse and non-symmetrical, making calculations difficult.

The sequential deposition in our model provided a numerical solution to determine a good candidate for this distribution. As shown in eqn (50), the segment length distribution for one-sided contacts between particles is given by a convolution of two positively supported functions $f_0 \coloneqq \mu \mathrm{e}^{-\mu x}$ and $g \coloneqq f_{d_{12}}$. With the one-sided distributions $f_{l_s} \coloneqq h(x) = (f_0 \otimes g)(x)$, it is possible to approximate the particle size PDF $f_{d_{12}}$. Using the convolution theorem for discrete functions[2], we can express this PDF in the form

$$f_{d_{12}} \coloneqq g = \mathrm{DFT}^{-1}\left[\frac{\mathrm{DFT}\,[h]}{\mathrm{DFT}\,[f_0]}\right], \tag{57}$$

[2] This can of course also be done for continuous functions, but our measured segment-length distributions consisted of normalized discrete histograms.

where DFT is the discrete Fourier transform. A solution of this kind is shown in fig. 8a. As expected, an exact deconvolution is very sensitive to noise in the data, and the result is neither smooth nor a proper PDF (as it contains negative values). We used thus Gaussian smoothing of the simulated data to get a smoother function h' (and thereby respectively g'). Now we have a two parameter regression problem to solve in order to find the g', with arguments μ and σ. Regression was made in a traditional 'least-squares' manner, but we added two regularization terms in the cost function, viz. one to ensure the smoothness of function g' and another to ensure process frequency $\mu = (\langle l_s \rangle - \langle d \rangle)^{-1}$, such that

$$G = \Sigma \left(h' - h\right)^2 - \lambda_1 \Sigma \left(g'_{n+1} - g'_n\right)^2 + \lambda_2 (\mu - (\mathrm{EV}[h] - \mathrm{EV}[g])^{-1})^2, \tag{58}$$

where EV denotes an expected value and g' is given by

$$g' = DFT^{-1} \left[\frac{\mathrm{DFT}\,[h']}{\mathrm{DFT}\,[f_0]} \right]. \tag{59}$$

A result of smoothing is shown in fig. 8b, where we show the original data h, the 'smoothed' data h' and the steric PDF $g' = f_{d_{12}}$ obtained by eqn (57). We show furthermore a best fit to the obtained distribution of steric hindrances by the expression

$$f_{d_{12}}(x) = \frac{x}{\langle d \rangle^2} \mathrm{e}^{-\frac{x}{\langle d \rangle}}; x \geq 0, \tag{60}$$

i.e. the convolution of two negative-exponential distributions. This type of distribution is more commonly known as an Erlang distribution with a shape factor of two.

In practice, the choice of a good candidate for the steric hindrance is ambiguous and many different PDFs give reasonable or good results. The main reasons for using a negative-exponential distribution for particle sizes were that a negative exponential distribution is positively supported (use of e.g. a Gaussian distribution is limited to its truncated version as particle sizes cannot be negative). Its functional form is also close to that of the segment length distribution making an analytical solution easier. In addition, perhaps coincidently, the PDF is now controlled by only one parameter making regressions to experimental data more robust.

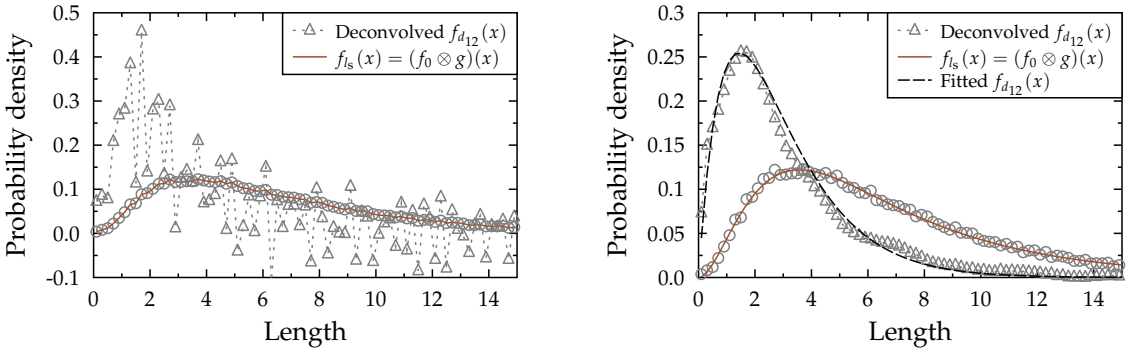

(a) Non-regularised (b) Regularised

FIGURE 8 (a) A non-regularised deconvolution of a one-sided segment length distribution. The result of a deconvolved steric hindrance, i.e. eqn (57), is shown as a dashed line. (b) Least squares regression of the cost function of eqn (58) with h (circles), h' (solid line) and g (triangles) . The dashed black line shows the best fit to the contribution of steric hindrances by eqn (60).

4.2 Coordination number distribution

For the coordination number distribution we could not find or derive a solution for the disperse Tonks gas. However, the regular Tonks gas can still be used to model a steric hindrance in the formation. The probability of finding N particles of diameter d in a fixed length L can be expressed in the form (Robledo and Rowlinson, 1986)

$$P(C = N) = \frac{Z(N, L/d)\zeta^N}{\Xi(\zeta, L/d)}, \tag{61}$$

where (the reduced activity) $\zeta = \frac{n}{n-1} \exp\left(\frac{n}{1-n}\right)$ with $n = \langle C \rangle d/L$. The grand partition function is $\Xi = (1-n) \exp\left[(L/d+1)\, n/(1-n)\right]$ in the limit $L/d \gg 1$ and the partition function Z is given by

$$Z = \begin{cases} (\frac{L}{d} - N + 1)^N / N! & ; N \leq \frac{L}{d} + 1, \\ 0 & ; N > \frac{L}{d} + 1, \end{cases} \tag{62}$$

and we find that the distribution of coordination number C in the one-sided process is given by

$$P_1(C = N) = \frac{\left[(\frac{n}{1-n})(\frac{L}{d} - N + 1)\right]^N}{(1-n)N!} \exp\left[-n/(1-n)(L/d + 1 - N)\right]. \tag{63}$$

The exact solution for $n = \{2, 3, \ldots\}$ superposed processes are given by the convolutions $P_n(C = N) = P_1(C = N) \otimes P_{n-1}(C = N)$ but are omitted here, as no analytic solution was found for any $n > 1$. Eqn (63) seems to be a good approximation as the convolution preserves the shape of the function. For reasonable parameters, the one-sided distribution can be fitted to the two-sided distribution with an accuracy of four digits. As a rule of thumb $P_n(\langle C \rangle, nd) \approx P_1(n\langle C \rangle, d)$.

4.3 Geometrical mapping of a Tonks gas

After establishing a theoretical model for the effect of the steric hindrance in contact formation, we now proceed to discuss the effect it may have on mean properties of the network.

The simplest way of mapping the sterically hindered process from a 1D process into a geometric structure in $\mathbb{R}^3$ is to simply expand it in such a way that the Point process is preserved. We thus consider a structure made of layers of parallel (stiff and long) fibres stacked on top of each other, so that successive layers cross each other in a right angle. When the network is constructed in this way, we can introduce the same steric hindrance for each fibre as in the Tonks gas model (the contacts in each fibre are formed by two independent sterically hindered point processes) as long as $f_{d_{12}}(x) = 0$ for $x < W$.

4.3.1 Mean values

By dividing this (rectangular lattice structure) into cuboids, each cuboid containing one contact, the contact density is given by the inverse of the average cuboid volume,

$$\rho_c = \frac{1}{\langle l_{s1} \rangle^2 H}, \tag{64}$$

where H is the height of the fibre (we keep the height as a separate variable, as e.g. cellulose fibres with a collapsed lumen tend to be more or less flat) and $\langle l_{s1} \rangle$ is the mean one-sided segment length. The fibres of one layer will on the average be separated by a distance of $\langle l_{s1} \rangle$, and assuming that $L \gg W$, the solids content of a layer is given by

$$\phi_s = \frac{A_f}{\langle l_{s1} \rangle H}. \tag{65}$$

Combining this expression with eqn (64), we find that the contact density for this type of structure is given by

$$\rho_c = \phi_s^2 \frac{H}{A_f^2}. \tag{66}$$

We can now adjust the contact density by, instead of placing layers in a right angle to each other, rotating successive layers by arbitrary angles $\theta_i \in]0, \pi[$, while the point process is kept intact. This means that the cuboids deform into right parallelogram prisms, and the contact density is now given by

$$\rho_c = \frac{\langle \sin\theta \rangle}{\langle l_{s1} \rangle^2 H} = \frac{1}{4 \langle \sin\theta \rangle \langle l_s \rangle^2 H}, \tag{67}$$

where $\langle l_s \rangle$, the mean segment length between contacts from both sides of the fibres, is now determined from the rotated layers. Note that now the distribution of segment lengths is changed as individual one-sided segments between two

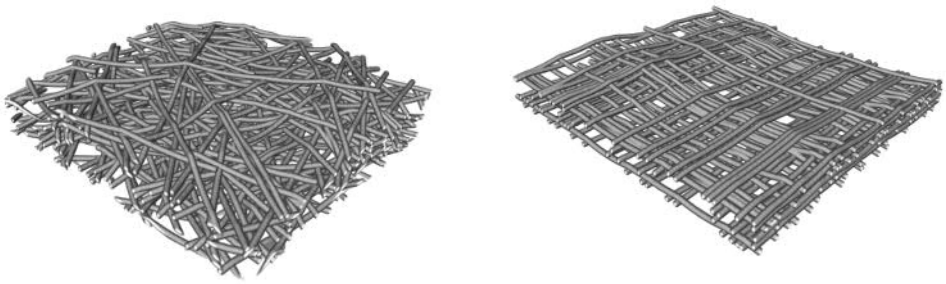

(a) Random deposition network (b) Geometrical map

FIGURE 9 A numerically generated deposited network (a) and its corresponding geometrical map of the ontact formation (b). Both structures have similar density $\phi_s \approx 0.1$ and mean segment length $l_s \approx 4W$.

layers get longer by a factor of $(\sin\theta)^{-1}$. As the point process was kept intact, the density is the same and thus the contact density is given by

$$\rho_c = \phi_s^2 \frac{H\langle \sin\theta \rangle}{A_f^2}, \tag{68}$$

which is of the same form as for uncorrelated infinitely-long cylinders. The difference is that now we have a geometrical structure that incorporates the steric effects between the fibres.

The next step is to incorporate a finite length of the fibres in the model, and we consider here its two modifications by cutting the infinite fibre into finite pieces. The equations in the case that the cutting produces finite fibres which are not in contact are identical to those of infinitely long fibres, otherwise, we introduce a correction which depends on the number density of the fibres, i.e.

$$\rho_c = \phi_s^2 \frac{H\langle \sin\theta \rangle}{A_f^2} + \rho_f. \tag{69}$$

This type of correction can also be made in our structure such that only a fraction of the fibres are separated. In this way we have a way of constructing a general polynomial of capped cylinders of finite length in the form

$$\rho_c = a\frac{\phi_s^2}{A_f^2}H + b\frac{\phi_s}{V_f}, \tag{70}$$

where the two parameters ($a \in]0,1]$ and $b \in [0,1]$) can be adjusted by rotating successive layers (a) and by separation of fibre ends (b).

4.3.2 Indirect measuring – shortest path analysis

With the geometrical mapping of the contact forming process to $\mathbb{R}^3$ we have well determined the structure for which relevant characteristics can be adjusted to

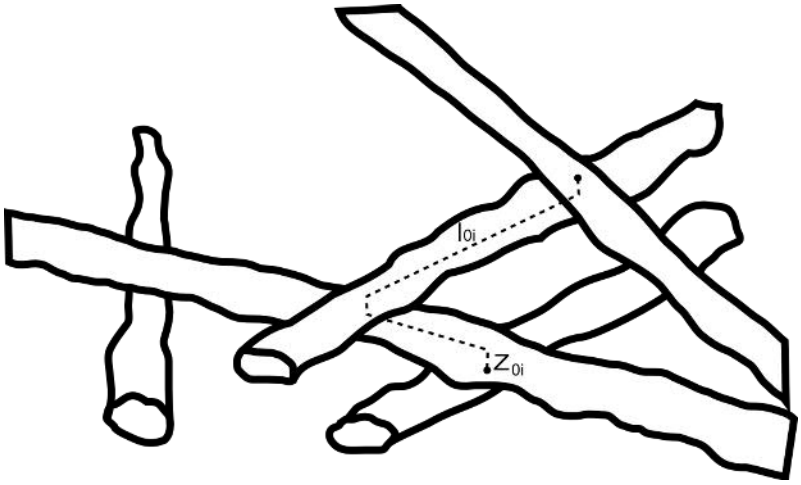

FIGURE 10 If the z-orientation in the fibre network is negligible, the only displacements in the z-direction along a path through fibres appear at fibre-fibre contacts

those of real deposited fibre networks. This enables indirect measurements of the structure, which one hopes to correlate with the corresponding properties in true random networks.

One such method is introduced in Publication I. Regrettably, the theory of contact formation was not fully developed, and a simplified version of the one-sided segment length distribution was used. Even though we provide here a more general solution, now including steric hindrance, results utilising this knowledge are not available.

Consider paths along fibres in the structure through the network (perpendicular to the fibre layers). As the layered structure of our structure produces a truly planar fibre orientation it thus follows, that paths travel along segments and through contacts to the next layer of fibres. Assuming that combinatorics play only a minor role along these paths, we assume that they always follow the shorter of the two possible segments to the adjacent contacts on the other sides of the fibres. For a uniform distribution along the length between adjacent contacts on one side of the fibre, excluding dangling ends, the expected value for the horizontal distance to the nearest contact is $l_{s1}/4$, where l_{s1} is the distance between the adjacent contacts on the other side of the fibre.

The distribution of the segment lengths along which the shortest path will propagate is not given directly by the segment length distribution, as the probability for a contact to be located between two contacts on the opposite side separated by distance X is proportional to the length of the segment. For a uniform distribution of events along the fibre, this probability is given by $f_X = cxf_{l_s}(x)$, where c is the linear contact density. Assuming a constant contact depth z_0, we find that the expected value of p_i is given by

$$\langle p_i \rangle = \int_0^\infty f_X(x)\sqrt{(x/4)^2 + z_0^2}\,\mathrm{d}x, \tag{71}$$

where $f_X(x)$ is the PDF for the geodesic curve between two contacts of length $\sqrt{(x/4)^2 + z_0^2}$. We express the segment length distribution in the form

$$f_{l_{s1}}(x) = \sum_{j,k} a_{j,k} x^j \mathrm{e}^{-\mu_k x}. \tag{72}$$

With the substitutions $y = \frac{x}{4z_0}$ and $t_k = 4\mu_k z_0$ we can express eqn (71) in the form

$$\frac{\langle p_i \rangle}{z_0} = \int_0^\infty \left[\sum_{j,k} b_{j,k} y^j \mathrm{e}^{-t_k y} \right] \sqrt{y^2 + 1^2}\, \mathrm{d}y. \tag{73}$$

So as to solve eqn (73), we begin by noting that (Gradshteyn and Ryzhik, 1965)

$$F(\mu, \beta) := \int_0^\infty \frac{x \mathrm{e}^{-\mu x}}{\sqrt{x^2 + \beta^2}}\, \mathrm{d}x = \frac{\beta\pi}{2}[H_1(\beta\mu) - N_1(\beta\mu)] - \beta, \tag{74}$$

where $H_1(\beta, \mu)$ is the first-order Struve function and $N_1(\beta, \mu)$ is the first-order Neumann function (Abramowitz and Stegun, 1972) with the constraints for the constants $|\arg \beta| < \frac{\pi}{2}$ and $\mathrm{Re}(\mu) > 0$. By choosing $\beta = 1, \mu = t$ and integrating by parts, we find that

$$F(\beta, \mu) = \left[\mathrm{e}^{-tx} \sqrt{x^2 + 1} \right]_0^\infty + \int_0^\infty t \mathrm{e}^{-tx} \sqrt{x^2 + 1}\, \mathrm{d}x, \tag{75}$$

from which we find the solution

$$\int_0^\infty \mathrm{e}^{-tx} \sqrt{x^2 + 1}\, \mathrm{d}x = \frac{F(t, 1) + 1}{t} \equiv G(t, 1). \tag{76}$$

The partial derivatives of $G(t, 1)$ can now be expressed in the form

$$\int_0^\infty x^n e^{-tx} \sqrt{x^2 + 1}\, \mathrm{d}x = (-1)^{n+1} \frac{\partial^n}{\partial t^n} G(t, 1), \tag{77}$$

and eqn (73) can be expressed in the form

$$\frac{\langle p_i \rangle}{z_0} = \int_0^\infty \left[\sum_{j,k} b_{j,k} \frac{\partial^j}{\partial t^j} G(t_k, 1) \right]. \tag{78}$$

The needed derivatives of the modified Bessel functions are given by the recursive relations (Abramowitz and Stegun, 1972, p. 361)

$$\frac{\partial}{\partial x} N_n(x) = -N_{n+1}(x) + \frac{n}{x} N_n(x) \tag{79}$$

and (Abramowitz and Stegun, 1972, p. 496)

$$\frac{\partial}{\partial x}H_n(x) = \frac{1}{2}\left(H_{n-1} - H_{n+1} + \frac{(\frac{1}{2}x)^{n+1}}{\sqrt{\pi}\Gamma(n+\frac{3}{2})}\right). \tag{80}$$

For a simple negative-exponential distribution, we can express the solution eqn (78) in the form

$$\frac{EV(p_i)}{z_0} = \frac{\pi}{2}\left[H_1(t) - \frac{t}{2}\left(H_0 - H_2 + \frac{t}{2\sqrt{\pi}\Gamma(\frac{5}{2})}\right) - tN_2(t)\right]. \tag{81}$$

These paths can then be measured from e.g. tomographic images of fibrous structures as shown in section 5.

5 EXPERIMENTAL AND NUMERICAL NETWORKS

The applicability of a theoretical model is questionable without proper validation against experimental data, as it is difficult to properly determine whether the underlying assumptions are correct or sufficient to describe the problem at hand.

This chapter is dedicated to the experimental and numerical work. We introduce our experimental samples, as well as the analysis made on them. Additionally we go through our decisions and simplifications concerning the numerical work, i.e. the computational deposition model built to address our problem. A short description on the non-dynamical deposition used in Publications I and II is given in the appendix of Publication I and is not covered here.

5.1 Fibrous networks

We first introduce the common image process analysis done for all the fibrous samples in our study. All reconstructed tomographic images were filtered for noise using a 3D variance based filter (Gonzales and Woods, 1993). This filter measures the standard deviation of gray-values in a region of specified size in the image. The executed convolution then depends on the variance so that, if it is large compared to a set threshold, the executed convolution is small, and vice versa. As a result of this kind of filtering edges are preserved, but the noise in homogeneous areas is reduced.

The samples were then rotated manually so that the planar network lay parallel to the xy-plane. From this processed image a region was manually selected from the middle of the sample, so that the selection did not include any cut marks, bended edges or otherwise unsuitable features. Finally the 'Magic Carpet algorithm' (Turpeinen et al., 2015) was used to detect the both top and bottom surfaces of the sample, respectively.

5.1.1 Cardboard samples

For Publication I our sample set consisted of a set of eight uncalendared, machine made, cardboard samples. The calibration of a correct threshold gray value for these samples was made by linking it to the grammage, i.e. the areal mass density of the samples. As the samples were machine made, it provided a very reliable measurement for calibration. The grammage of an image can be expressed in the form

$$\rho_{\mathrm{m}}\rho_A = \rho_{\mathrm{m}} \sum_i \phi_{\mathrm{s}i} s, \tag{82}$$

where $\phi_{\mathrm{s}i}$ is the solids content of the xy-plane i of the image, s is the voxel unit length, and ρ_{m} is the fibre material (cell-wall) density. Based on literature values (Niskanen et al., 1997) we chose a density of 1500 $\mathrm{kg/m^3}$.

After the binarisation of the images, the surfaces were detected using the method described by (Turpeinen et al., 2015) resulting in two functions $Z_{\mathrm{top}}(x, y)$ and $Z_{\mathrm{bottom}}(x, y)$ describing the surface topology of the sample. The shortest path was then taken between the two planes described by the mean values $\langle Z_{\mathrm{top}}(x, y)\rangle$ and $\langle Z_{\mathrm{bottom}}(x, y)\rangle$.

The mean shortest path between any two planes in the sample is not necessarily symmetric. This is obvious if the two planes have a different amount of solids content, i.e. $\phi_{\mathrm{sA}} < \phi_{\mathrm{sB}}$, as the shortest paths from plane B to plane A will be mapped on a subset A' of the voxels in plane A. Now all the remaining voxels $A \setminus A'$ will by definition have a longer path to plane B than any of the paths from B to A, and thus than any of the paths from A' to B. Owing to this, the measurement of the shortest paths along the fibre materials used for the calculation of segment length was taken as the average of the values for both directions.

5.1.2 Foam-formed samples

Publications (III; IV; VI) all deal with the same sample series. This series was a test series using foam as the carrier fluid in the forming process of the sheets. The sample series consisted of two different fibre materials (Kraft and CTMP) with varying bubble radii of the suspending fluid. Both series had a reference sample manufactured with water-forming.

In this sample series the main focus was on the void space distribution of the networks. To this end, extra attention was paid to ensure that the void space was clean. With this we mean that distance transforms in 3D images are very prone to noise, and even a single solid voxel in the void space has a drastic effect on e.g. its thickness.

The void structure of the networks was characterized with their local thickness using the implementation by Dougherty and Kunzelmann (2007) (see section 3). Additionally, the lattice-Boltzmann (LB) method (Chen and Doolen, 1998; Aidun and Clausen, 2010; Mattila et al., 2016) was used for simulating fluid flows directly

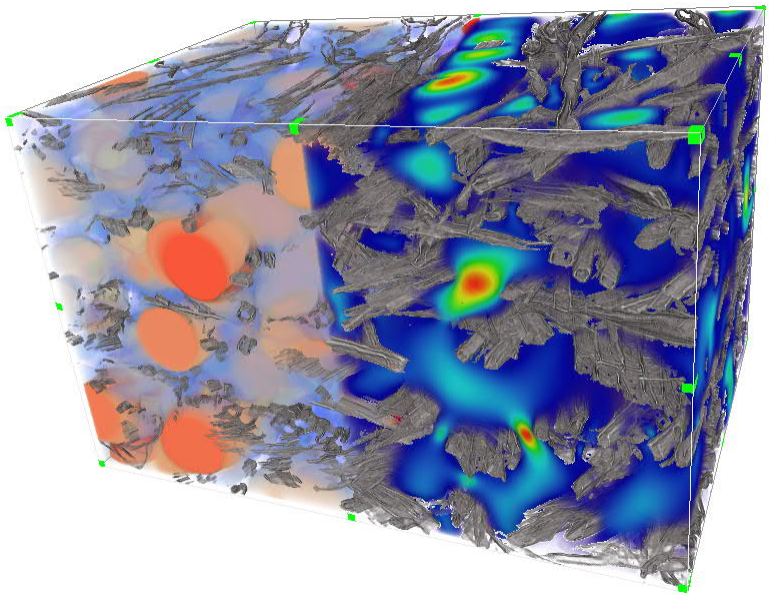

FIGURE 11 A cropped sample of a tomographic images of a foam-formed network. As a local measure for the void space we used the local thickness, i.e. the size of the largest sphere fitting completely into the void (left side). Numerical solutions to the transverse fluid flow were determined for the same geometries (right side).

in the pore structures given by the tomographic images.

5.2 Granular sample

Detailed information about short-cut spaghetti does, unfortunately, not yet have any direct applications and the usefulness of its study may be questioned. Detailed information on the connectivity of commonly used materials would of course be more industrially applicable, but as of now, it seems that the image analysis is not developed enough for accurate determination of contacts, and has only been (reliably) done in very specifically manufactured samples (Marulier et al., 2012), structures with high contrast (Tsarouchas and Markaki, 2011) and dilute systems such as fibre reinforced composites (Shen et al., 2004; Lux et al., 2006) or foams (Elliott et al., 2002; Montminy et al., 2004; Dillard et al., 2005).

The short-cut spaghetti strands were chosen as they were readily available, industrially made (thus have a very consistent geometrical shape) and relatively cheap. Similar tests were done with hand-cut copper wire but they proved to be not as suitable. Moreover, this work follows the tradition on using food products in the study of granular material (Frette et al., 1996; Donev et al., 2004; Blouwolff and Fraden, 2006; Denisov et al., 2012; Kyrylyuk et al., 2011).

5.2.1 Preparation

As de Gennes (1999) mentioned, even the simple task of sample preparation, 'We fill a cylinder with sand', hides many subtle but important details. Even with spherical particles, one is able to produce many different densities of random packing. With higher aspect ratio constituents, this becomes even more important, owing to the additional problem of orientational ordering, especially near the container walls. In our experiments our sample preparation consisted of pouring the same amount of (short-cut) spaghetti into a cylindrical container while keeping track of the bulk height of the pile. The final pile was chosen from such a pouring that resulted in a relatively high pile. This was done to ensure that the chosen piles were as isotropic as possible, as nematic ordering of strands lead to denser piles.

The final piles were imaged with a SkyScan 1172 μCT scanner. All the samples were oversized and had to be scanned with parallel camera positions in three different stacked scans making this probably the largest tomographic reconstruction of spaghetti ever to be done, the raw data being a bit short of 100 GB in size. Needless to say, the actual analysis was made for scaled-down versions of this original data.

5.2.2 Image analysis – binarisation

As discussed earlier, the edges around objects tend to be smooth, and proper binarisation of the image is not always straightforward (Kerckhofs et al., 2008). As an independent measurement, a separate set strands were measured for their length and thickness. This measurement was then used to aid in the image processing.

The binarisation process $B(\sigma, T)$ consisted of a Gaussian convolution with a kernel size σ and a gray-value thresholding of T into a binarised image (void and solids). The final parameters were chosen so that the thickness of the strands matched that of the calibration measurement D_{calib}. The smoothing was a necessary step to minimize the amount of holes (from both imaging noise and manufacturing defects of the spaghetti) in the binarised image, as existence of these kinds of holes complicates the segmentation process[1]. The thickness alone is not sufficient to fix the parameters σ and T, as for large enough σ one can adjust the mean local thickness almost arbitrarily. For each tomographic image an optimal pair of parameters σ and T was chosen such that the resulting local thickness of the binarised image was equal to the measured thickness of the spaghetti and its standard deviation was minimized. An example of this calibration step is shown in fig. 12.

[1] A single pixel hole affects the EDT of the solids in such a way, that the strand is often cut into two parts.

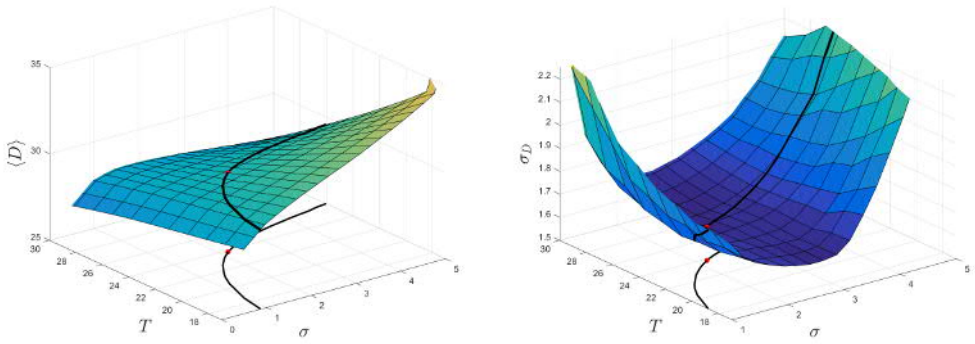

(a) (b)

FIGURE 12 The binarisation of the tomographic images was done by measuring (separately) the thicknesses of the spaghetti strands. The binarisation process, i.e. a Gaussian convolution with radius σ and a gray value thresholding with value T resulted in an average value for the thickness of the strands measured from the tomographic images (a). From the curve satisfying $D(\sigma, T) = D_{\text{calib}}$, shown in black, we chose the pair (σ, T) minimizing the standard deviation (b) of the thickness distribution (red dot).

5.2.3 Image analysis – segmentation

The steps in the segmentation process are shown in fig. 13. After the binarisation of the gray-scale imaging a Euclidean distance transform was applied on the solids (distance to the void). This distance transform was thresholded such that most contact boundaries were erased, but the center of the strands were intact. The resulting disjoint set of voxels were labelled and then dilated (simultaneously) in the binarised images.

As mentioned earlier, holes in the strands, both from actual structural defects such as fractures and from imaging artefacts, make it difficult to obtain a set of parameters such that the segmentation is without errors. This causes some strands to be (falsely) divided into two or more parts, and some strands to be fused together. We found that a good method to determine whether strands were properly segmented was by comparing the lengths of their medial axes. All mean values for the packing were then taken only using a subset of the fibres with the condition, that it and all its neighbours lengths deviate no more than two standard deviations from the mean. As shown in fig. 14, actual faults were rare, and the errors were mainly caused by the limited field of view of the μCT device. Nevertheless, the coordination numbers of those strands were systematically smaller and thus, rightfully so, were discarded.

The contacts were determined from the labelled image by going through each of the differently labelled strands in the image and listing all its unique 26-connected neighbours. As all strands were given a different label, this list produces a sparse-matrix representation of the connected graph of strands. Mapping these contacts onto the centreline of the fibre was done by extracting the medial axis of each

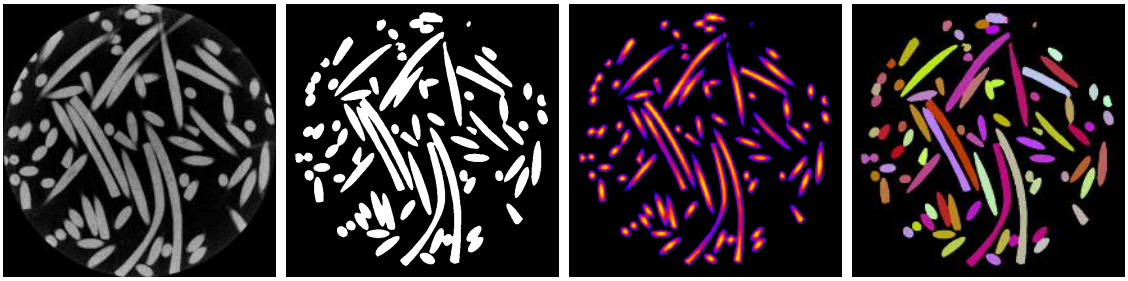

(a) (b) (c) (d)

FIGURE 13 (a) A gray scale image stack was (b) filtered and binarised. (c) A Euclidean distance transform (EDT) was applied to the binarised image. Local maxima of EDT were separated and diluted simultaneously in the existing binarised image, resulting in (d) an image of separately labelled spaghetti strands.

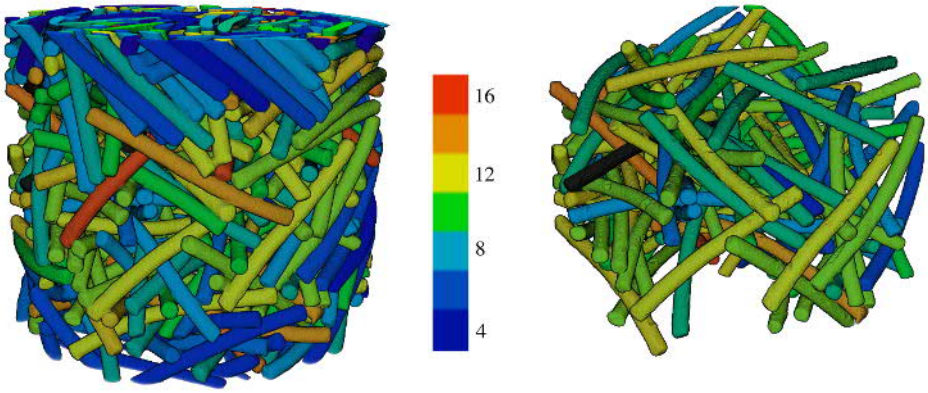

(a) (b)

FIGURE 14 Vizualizations of a random pile of spaghetti showing (a) all strands and (b) the 'good' strands used for calculating the results. Colour indicates the coordination number of the strands.

strand. Contact pairs between two strands were then determined by finding the minimum distance between their medial axes. The segment lengths were determined along these medial axes of the strands.

5.3 Numerical simulation

Experimental methods for contact detection in random piles are somewhat lacking and require often substantial manual labour. The famous example of this was reported by Bernal (1964), who conducted experimental work on the random packing of spheres. The experiment involved pouring paint over a container, letting it dry, and manually deducing the coordination number distributions from the trace of the dried paint. The same kind of experiment has later been performed

with both oblate (Donev et al., 2004) and prolate (Blouwolff and Fraden, 2006) objects.

As the experiments are difficult, many have turned to numerical models and these have been utilised for various purposes. A 3D version of drawing lines on a plane is a sequential deposition of sterically hindered fibres. This has been a starting point for many simulations. The fibres are deposited one by one on a (initially flat) substrate, letting bend by some predefined manner. After the fibre geometry is calculated, its position is fixed and it is added to the substrate. These kinds of non-dynamical networks generation are fast and provide suitable geometry for structural analysis (Niskanen and Alava, 1994; Hellen and Alava, 1997). Additionally they provide the structural geometry enabling determination of properties such as permeability (Koponen et al., 1998), diffusivity (Hellen et al., 2002) and elasticity (Åström et al., 2000a,b; Kulachenko and Uesaka, 2012). This type of sequential packing was used in Publications I and II.

Dynamic models of fibre deposition are more challenging and, as they are computationally more demanding, have usually been done on much smaller systems. Even recent papers deem the simulation of flexible fibres as numerically impractical (Nan et al., 2014). Nevertheless, many different models have been developed for many fields of research e.g. for fibre suspensions (Switzer and Klingenberg, 2004; Lindström and Uesaka, 2007, 2008) or for mechanical properties of networks (Switzer et al., 2004; Rodney et al., 2005; Barbier et al., 2009a,b; Subramanian and Picu, 2011). Although most numerical models of granular matter concern shorter aspect ratio particles, some work has also been done in this field for longer rods (Williams and Philipse, 2003; Wouterse et al., 2009).

Over the past years the numerical tools have been substantially developed in the field of graphics simulation, and moreover, modern computers can nowadays handle large systems enabling numerical modelling of systems of relevant macroscopic sizes. A nice overview on the subject can be found in the recent review on rigid-body simulations by Bender et al. (2013) and frameworks for fibres are readily available (Spillmann and Teschner, 2007, 2008; Bergou et al., 2008; Bertails-Descoubes et al., 2011; Daviet et al., 2011). This section is dedicated to presenting the underlying choices and details in the implementation used in our numerical model.

5.3.1 Kirchhoff rods

The Kirchhoff rod can be thought of as a geometrically non-linear generalization of an Euler-Bernoulli beam. It is a mathematical representation of a 3D elastic body with a large aspect ratio (two of its dimensions are much smaller than the third).

We will present here a short theoretic overview adapted from Singer (2008). The

configuration of an arbitrary rod can be described by a curve

$$\Gamma = \{\boldsymbol{\gamma}(s), \boldsymbol{T}(s), \boldsymbol{M}_1(s), \boldsymbol{M}_2(s)\}, \tag{83}$$

where $\boldsymbol{\gamma}$ is the parametrized curve in $\mathbb{R}^3$ and $\boldsymbol{T}(s), \boldsymbol{M}_1(s), \boldsymbol{M}_2(s)$ form an orthonormal material frame. The material frame is adapted to the centreline of the fibre, such that

$$\boldsymbol{\gamma}'(s) = \boldsymbol{T}(s). \tag{84}$$

The behaviour of the material frame along the curve is described by the Darboux vector $\boldsymbol{\Omega} = m\boldsymbol{T} - m_2\boldsymbol{M}_1 + m_1\boldsymbol{M}_2$ satisfying

$$\begin{aligned} \boldsymbol{T}' &= \Omega \times \boldsymbol{T}, \\ \boldsymbol{M}_1' &= \Omega \times \boldsymbol{M}_1, \\ \boldsymbol{M}_2' &= \Omega \times \boldsymbol{M}_2, \end{aligned} \tag{85}$$

and the strain along the material frame curve is given by

$$\begin{aligned} m_1 &= \boldsymbol{T}' \cdot \boldsymbol{M}_1, \\ m_2 &= \boldsymbol{T}' \cdot \boldsymbol{M}_2, \\ m &= \boldsymbol{M}' \cdot \boldsymbol{M}_2, \end{aligned} \tag{86}$$

and the total energy is given by the integration

$$E(\Gamma) = \frac{1}{2} \int \alpha_1 (m_1)^2 + \alpha_2 (m_2)^2 + \beta (m)^2 \, \mathrm{d}s, \tag{87}$$

where α_1, α_2 and β are the material constants.

5.3.2 Discretisation

In our work we used the discretisation of the Kirchhoff rod as presented by Bergou et al. (2008) as it provided a simple framework containing all the necessary tools for our simulation. Here we describe the discretisation of the system of rods in a special case, i.e. for an initially straight twist-free rod, of the general Kirchhoff rod. The initially straight capped cylinder of length L and width W was discretised into n points $\boldsymbol{x}_i$ and line segments $\boldsymbol{e}^i = \boldsymbol{x}_{i+1} - \boldsymbol{x}_i$ (fig. 15) of length $l_0 = L/(n-1)$. The elastic energy of a rod is taken as a combination of a bending energy,

$$E_\mathrm{b} = \frac{1}{2} Y I \sum_{i=1}^{n-2} \frac{(\boldsymbol{\kappa} \boldsymbol{b}_i)^2}{l_0}, \tag{88}$$

where Y is the Young's Modulus and I is the area moment of inertia, and a stretching energy,

$$E_\mathrm{s} = \frac{1}{2} \frac{Y A_\mathrm{c}}{l_0} \sum_{i=1}^{n-1} (|\boldsymbol{e}^i| - l_0)^2. \tag{89}$$

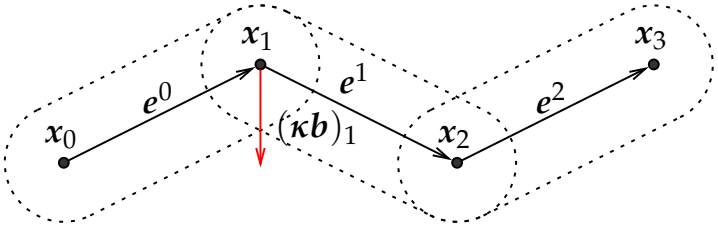

FIGURE 15 A discrete capped cylinder. The dotted areas represent the volume of interaction with other rods.

The curvature binormal at each vertex $(\kappa \boldsymbol{b}_i)$ is defined as by Bergou et al. (2008), i.e.

$$(\kappa \boldsymbol{b}_i) = \frac{2\boldsymbol{e}^{i-1} \times \boldsymbol{e}^i}{|\boldsymbol{e}^{i-1}|\,|\boldsymbol{e}^i| + \boldsymbol{e}^{i-1} \cdot \boldsymbol{e}^i}. \tag{90}$$

The forces that arise from the stretching are now given by one or both of the terms

$$\begin{aligned} \boldsymbol{F}_{i+} &= k\frac{\boldsymbol{e}^i}{|\boldsymbol{e}^i|}(|\boldsymbol{e}^i| - l_0) \text{ for } i \leq n-1, \\ \boldsymbol{F}_{i-} &= k\frac{\boldsymbol{e}^{i-1}}{|\boldsymbol{e}^{i-1}|}(l_0 - |\boldsymbol{e}^{i-1}|) \text{ for } i \geq 1, \end{aligned} \tag{91}$$

with $k = \frac{YA_c}{l_0}$, and the forces owing to bending energy are a sum of up to three contributions

$$\boldsymbol{F}_i = -\frac{YI}{2l_0}(\boldsymbol{\nabla}_i(\kappa \boldsymbol{b})_j)^T(\kappa \boldsymbol{b})_j, \tag{92}$$

with

$$\begin{aligned} \boldsymbol{\nabla}_{i-1}(\kappa \boldsymbol{b})_i &= \frac{2\left[\boldsymbol{e}^i\right] + (\kappa \boldsymbol{b})_i(\boldsymbol{e}^i)^T}{|\boldsymbol{e}^{i-1}|\,|\boldsymbol{e}^i| + \boldsymbol{e}^{i-1} \cdot \boldsymbol{e}^i} \\ \boldsymbol{\nabla}_{i+1}(\kappa \boldsymbol{b})_i &= \frac{2\left[\boldsymbol{e}^i\right] - (\kappa \boldsymbol{b})_i(\boldsymbol{e}^i)^T}{|\boldsymbol{e}^{i-1}|\,|\boldsymbol{e}^i| + \boldsymbol{e}^{i-1} \cdot \boldsymbol{e}^i} \\ \boldsymbol{\nabla}_i(\kappa \boldsymbol{b})_i &= -\left(\boldsymbol{\nabla}_{i-1} + \boldsymbol{\nabla}_{i+1}\right). \end{aligned} \tag{93}$$

5.3.3 Fibre-fibre interactions

To implement the actual steric hindrance between our flexible fibres we need to incorporate fibre-fibre interactions between them. As our focus was on static (relaxed) states of the network our collision detection and handling need to fulfil two criteria: A hard-core repulsion, such that fibres do not overlap, and a static friction, so that a stable network is achieved.

Our solution was an energy based repulsion. The contacts were equipped with an harmonic potential

$$E_{\mathrm{c}} = \frac{1}{2}\frac{Y A_{\mathrm{c}}}{W}\Delta c^2, \tag{94}$$

where Δc is the depth of the overlap of the rods. A benefit of this kind of contact definition is, that it directly defines a normal force for sliding friction between the segments. This kind of friction was mainly added to prevent nematic ordering of fibres, as shown in fig. 16. The model was adapted from Bridson et al. (2002).

The static friction was modelled by tangential springs that were added upon contact, and removed with the criteria of Coulomb friction. This kind of static friction was first introduced by Cundall and Strack (1979) and have been used by many others since [see e.g. (Shäfer et al., 1996) and (Zhu et al., 2007)]. Essentially it involves adding a friction force

$$\boldsymbol{F}_{\mathrm{s}} = -\min\left(\left|k_{\mathrm{s}}\boldsymbol{\zeta}\right|, \left|\mu\boldsymbol{F}_{\mathrm{n}}\right|\right) \cdot \operatorname{sign}\zeta, \tag{95}$$

where $\boldsymbol{F}_{\mathrm{n}}$ is the normal force of the contact, μ the friction coefficient and $\boldsymbol{\zeta}$ denotes the relative tangential displacement between the two particles since they first made contact. With the criteria of Coulomb friction, we mean that this tangential spring is deleted if $\left|k_{\mathrm{s}}\boldsymbol{\zeta}\right| > \left|\mu\boldsymbol{F}_{\mathrm{n}}\right|$ (slip) and if $\left|\mu\boldsymbol{F}_{\mathrm{n}}\right| = 0$ (lift off).

Constrain based hard-core interactions, such as in Goldenthal et al. (2007) and Spillmann and Teschner (2008), were tested but were found unsuitable. In a stable network of rods (by applying either a gravitational field or sufficient compressional force) the fibre network percolates, and the inversion of the constraint matrix dominated the simulation time. More exact methods for friction are also available, such as e.g. Bertails-Descoubes et al. (2011) and Daviet et al. (2011), but were found unsuitable for excessive computational demands.

The collision detection was made pairwise between fibre segments using the algorithm described by Vega and Lago (1994) using spatial hashing of the simulation space (Teschner et al., 2003). As collision detection was made pairwise, an additional filtering of contacts was needed so as to remove duplicate contacts owing to the overlapping 'contact volume' at the vertices $\boldsymbol{x}_i$ (see fig. 15). Duplicate contacts at these overlapping areas were removed by maintaining the contact with a larger overlapping distance.

A non-linear contact force, such as a Herzian contact, could easily be incorporated, but as our current version was developed to extract geometrical effects, this was not prioritised. For contacts between two cylinders, the relevant response is given by Puttock and Thwaite (1969).

An example of a compression of xy-periodic network of fibres is shown in fig. 17. In fig. 18 we show a simulated deposition of spaghetti strands compared to that of a tomographic reconstruction of an actual granular pile.

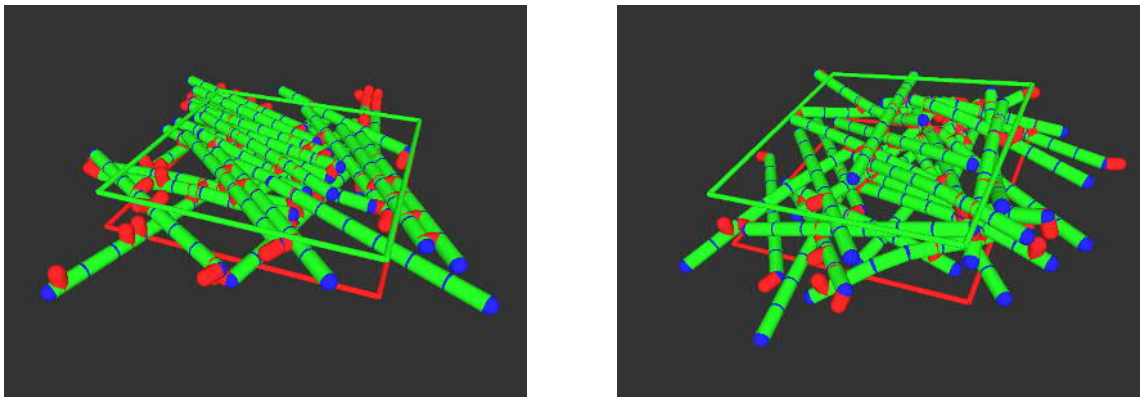

(a) Negligible friction (b) Friction

FIGURE 16 Example of the effect of the friction parameter on packing. (a) With neglible friction ($\mu = 2 \cdot 10^{-4}$) the rods are free to slide and thus the assembly tends to form a nematic ordering. (b) Introducing friction between the fibres ($\mu = 0.2$) preserves the isotropy of the orientation in the xy-direction.

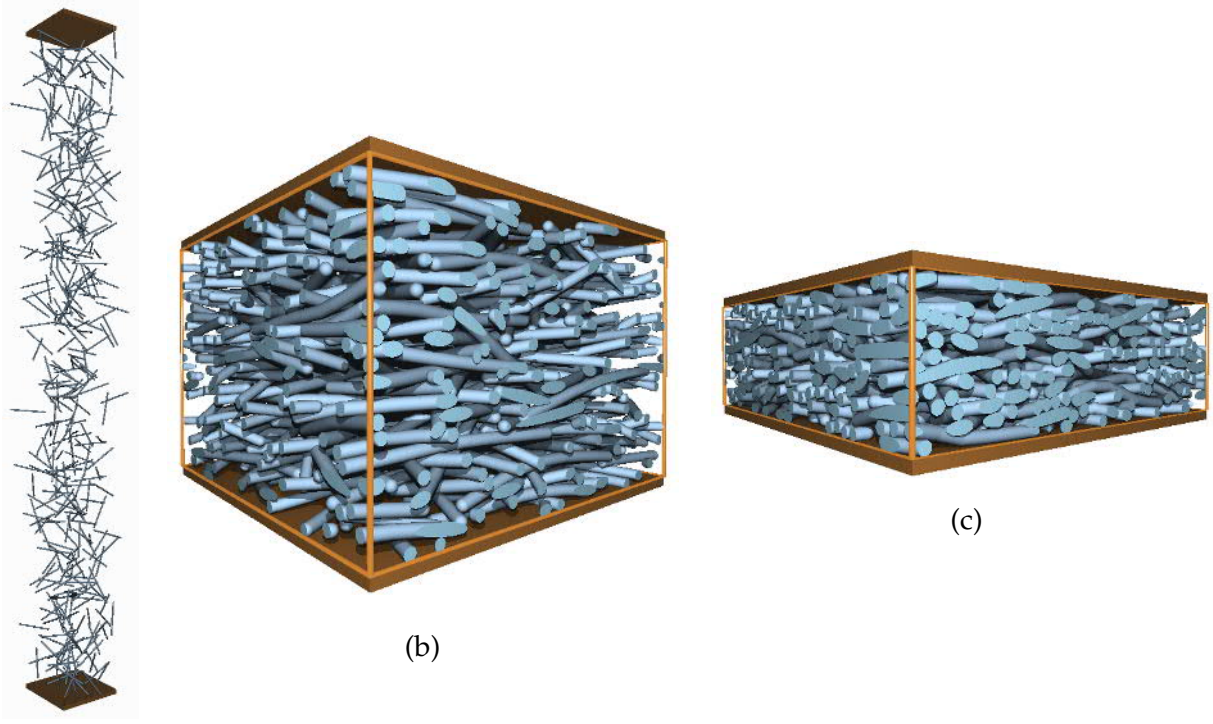

(a) (b) (c)

FIGURE 17 (a) Randomly packed networks generated by compressing an initial configuration of isotropically placed rods (L/W=20) between two plates. In (b), $\phi_s = 0.16$, and in (c), $\phi_s = 0.36$.

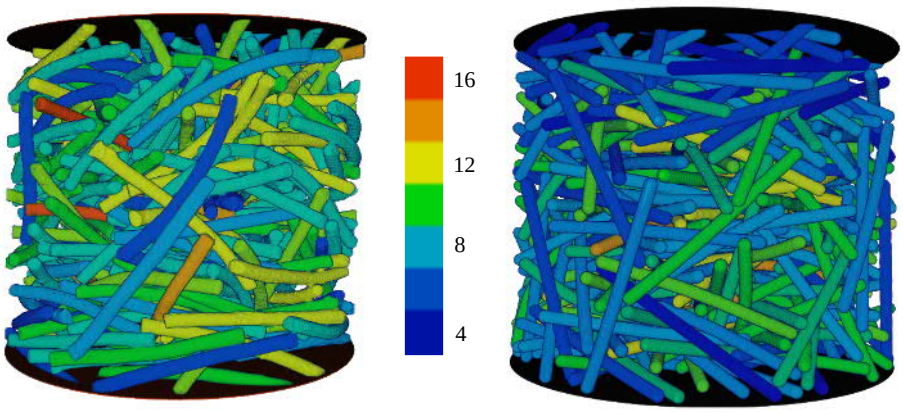

FIGURE 18 A random pile of short-cut spaghetti (left side) and a similar numerically generated random packing (right side). The colour indicates the coordination number of each individual object.

6 RESULTS

It this chapter we go through the results in the included publications most relevant to the theme of this Thesis, namely the effect of the steric hindrance.

We first summarise the results of contact formation, namely the resulting statistical distribution (Publication II). The properties of the global means are addressed (Publication V) after which the result of indirect measurement of one such property (Publication I) is presented. Lastly the steric effect by other factors than the network constituents themselves (Publication III,IV,VI) is addressed briefly.

6.1 Sterically hindered contact formation

In Publication II we presented a theoretic model for contact formation as a combination of two sterically hindered point processes on a 1D space. The developed theory was validated against both experimental and numerical results for random networks of both stiff and flexible fibres.

An effect noticed (which we address in more detail in Publication V) was that contacts at the ends of the fibres behaved differently compared to the other ones. As it is evident from fig. 19, the segment lengths including at least one fibre end (or a contact located at the fibre end) differ from the segments located more centrally in the fibres. An interesting observation was that this effect would go unnoticed without a detailed knowledge of the segment lengths as with a larger binning of the histogram, steric effects are concealed. All the distributions of segment lengths presented here are on the modified measurements, where end contacts are discarded, unless specifically mentioned otherwise.

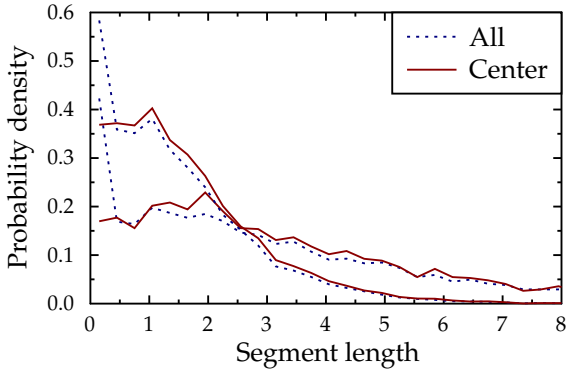

FIGURE 19 An example of the effect of the dangling ends on the segment length distribution for two networks of randomly deposited fibres. The segment length distribution of all segments (including the dangling ends) show a distinct peak of segments of vanishing length. After removing the segments which are located at the end of the fibres, the steric hindrance between the fibres is evident.

6.1.1 Segment length distribution

The numerically generated (sequentially deposited) networks provided a unique way to validate our theory, as the both one and two sided segment lengths were unambiguously determinable. An example of these two distributions is shown in fig. 20b and compared with that of a Poisson process. It is evident that the distribution for the one sided process is in excellent agreement with the measured segment lengths and that, moreover, both distributions show the behaviour of a negative-exponential tail, but a clear deviation from it at short segment lengths.

The effect of fibre flexibility on the distribution is shown in fig. 21. As expected, an increased flexibility of the fibres decreases the mean segment length, as the fibres can more easily bend to form more contacts. Flexibility also reduces the steric effect of fibres, which is also not surprising. Regardless of the flexibility, it is evident that all the observed distributions deviate substantially from that of an uncorrelated process, i.e. a negative exponential distribution.

The assumption for our model was that contact formation takes place in two processes. This is, as stated, well justified for strictly planar networks, where contacts form on the either top or bottom side of the fibres. This is not necessarily true for isotropic networks, as contacts in them can form also on the sides of the fibres. This is also true for an increasing flexibility, as single segments can have a non-planar orientation even if the fibre,on the average, will not. It is evident from fig. 22 that the two-sided approximation becomes progressively worse with increasing flexibility.

As new results (not included in the attached Publications II or V) in fig. 23 we report here also the segment length distribution taken from a compression cycle

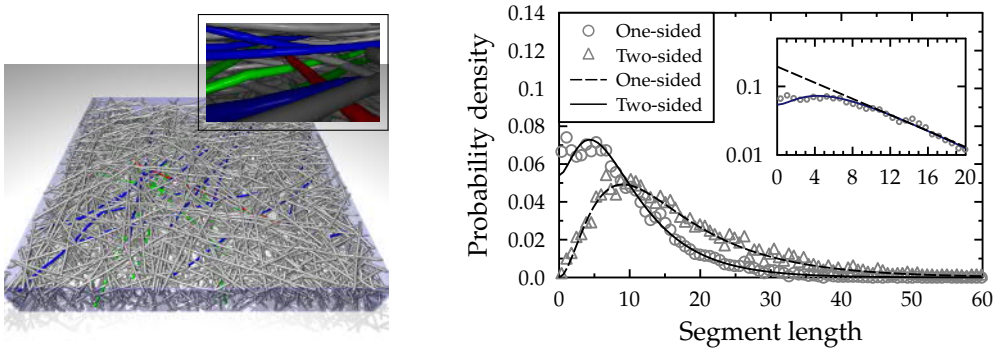

(a) (b)

FIGURE 20 (a) An example of numerically generated networks of sequential deposition utilised in Publications I and II. Upon contact with already deposited fibres (or the substrate), the lateral position of the deposited fiber was fixed, while it was allowed to bend to a pre-determined curvature. The chronological deposition of the fibers allowed us to distinguish contacts on the top (blue) and bottom (green) side of the deposited fibre considered (red). (a) Distributions of segment lengths between contacts on one side of a fibre and on both sides of fibres in a deposited network. The solid lines show the best fits to the numerical distributions of segment lengths as proposed in Publication II. The inset shows a comparison between the numerical two-sided distribution (all contacts) and a negative-exponential distribution. Although the numerical distribution has the characteristic negative-exponential tail, there is a notable deviation from it at small segment lengths. This deviation can be attributed to some kind of correlation between contacts, caused by the steric hindrances of fibres.

of the dynamic simulations. As the fibres in this case are allowed to slide and rearrange, the assumption of two-sidedness does not necessarily hold. Nevertheless, the distribution was very well described by the same functional form. A notable feature in the dynamical simulations, where fibres are allowed to slide, move and rearrange simultaneously, was the significantly lower steric hindrance. This is expected, as the neighbouring fibres can both rotate and bend to align more parallel to each other.

6.1.2 Coordination number distribution

In fig. 24 we show the coordination number distributions for networks made by sequential deposition. It is clear that the contact formation of the networks deviate significantly from that of an uncorrelated network. With this distribution we also fitted the data of Blouwolff and Fraden (2006) and these fits together with the data are shown in fig. 25. Fits of the experimental coordination number allow us to examine the steric effects in the contact formation of stiff rods. Fitting parameters are shown in table 2.

The theory was also tested against piles of short-cut spaghetti. Fits with theoreti-

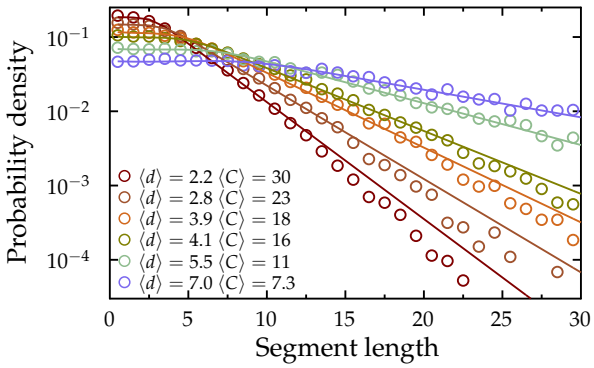

FIGURE 21 Segment length distributions and the corresponding best fits for a series of flexible fibres of aspect ratio $L/W \approx 100$. Stiffer fibres have a larger steric hindrance.

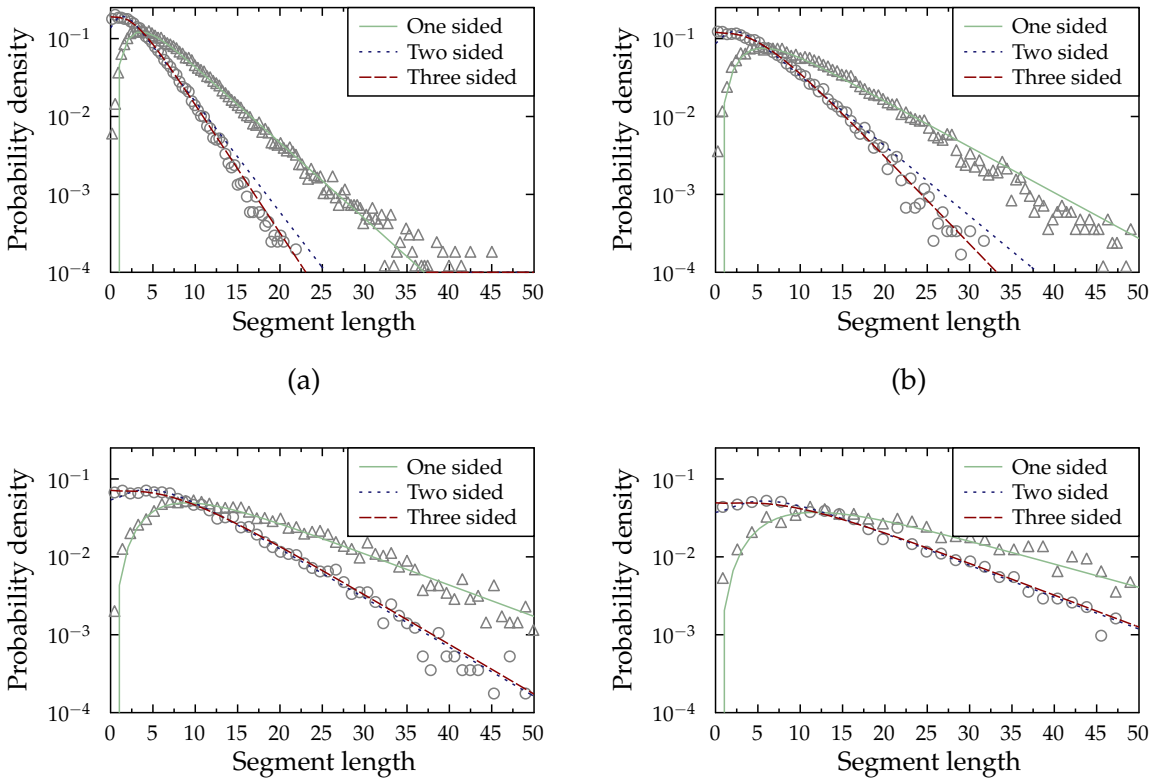

FIGURE 22 Fitted one- two- and three-sided segment length distributions for fibre networks for a stiffness increasing from the most flexible (a) to the most stiff (d) fibre. The one-sided distribution is in good agreement with all measured segment length distributions, while the two-sided distribution gets progressively worse for more flexible fibres.

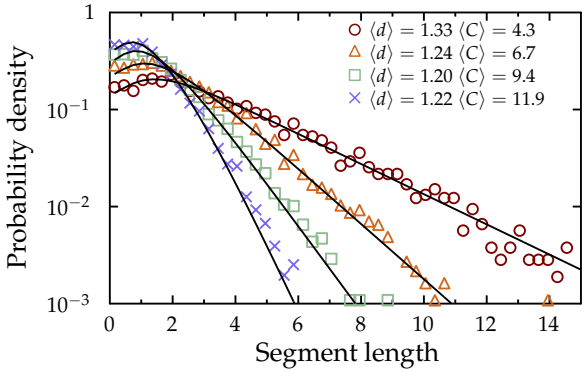

FIGURE 23 Segment length of the dynamic numerical model shows that compression decreases the steric hindrance between the fibres. This is an effect caused by both an increasing bending of the fibres as well as orientational ordering of fibre segments.

TABLE 2 Average coordination number (data from Blouwolff and Fraden (2006)) and particle size of the fitted two-sided Tonks gas distributions for uncompressed (unc.) and compressed (comp.) packings of rods shown in fig. 25.

L/W	50		32		16	
	unc.	comp.	unc.	comp.	unc.	comp .
C	8.1	9.7	7.4	9.7	6.5	7.0
d	4.2	2.7	3.4	2.8	2.1	1.7

cal distributions of the observed frequencies are shown in fig. 27. It is evident that both the segment length distribution and the coordination number distribution agree well with the measured results. Especially they both deviate significantly from that of an uncorrelated process.

It is evident from the results shown in table 2 that the steric hindrance $\langle d \rangle$ is larger than the rod diameter for rods of high aspect ratios. This implies that, although the non-zero diameter of the rods induces hard-core restrictions, the actual steric hindrance has a fibre orientation dependent component. As the rods are stiff and do not bend, the decrease of this hindrance upon compactification of the packing is suggestive of some kind of orientational ordering of adjacent crossing rods, i.e. neighbouring rods become more parallel on the average. So as to test the existence of local orientational order, we determined the distribution of the difference between the crossing angles in two adjacent contacts along individual fibres. In fig. 26 we show this distribution for both the numerical networks and the random pile of spaghetti. All these distributions indicate that there exists local nematic order between adjacent contacts along a rod even though the global orientation of the packings is isotropic.

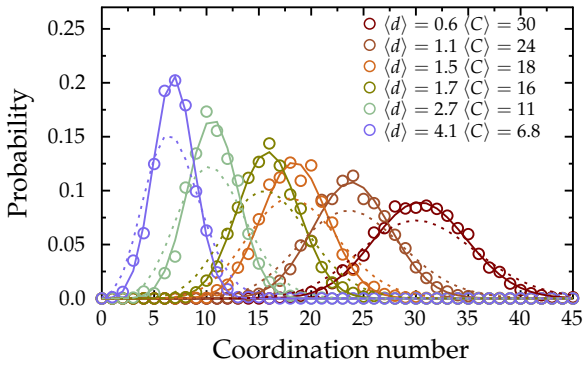

FIGURE 24 Coordination number distribution for the same series of numerically generated deposited networks as in fig. 21. Steric effects are evident by the deviation from a Poisson distribution (dashed lines).

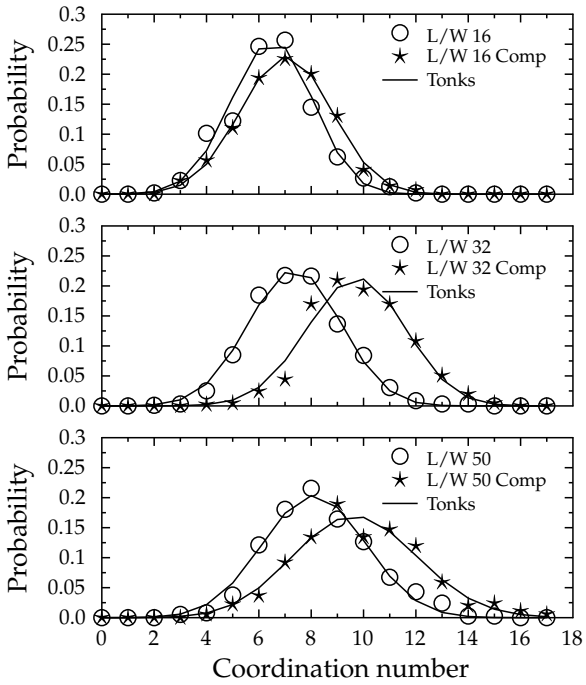

FIGURE 25 Coordination number distributions for the results of Blouwolff and Fraden (2006) for both their uncompacted and compacted piles. The fitting parameters of the Tonks gas are shown in Table 2. It is evident, that the compactification of the packing both increases the amount of contact, but also decreases the steric effect betweent he rods, thus suggesting a local nematic order between neighbouring rods.

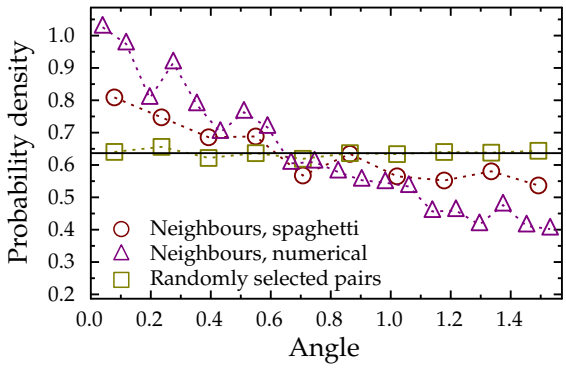

FIGURE 26 Distribution of the difference between the crossing angles in adjacent contacts along a rod of short cut spaghetti. So as to verify that no global correlation exists, a similar distribution was also determined for randomly selected pairs in the pile. Such a check was unnecessary for the numerically generated networks, as the planar orientation is isotropic by definition.

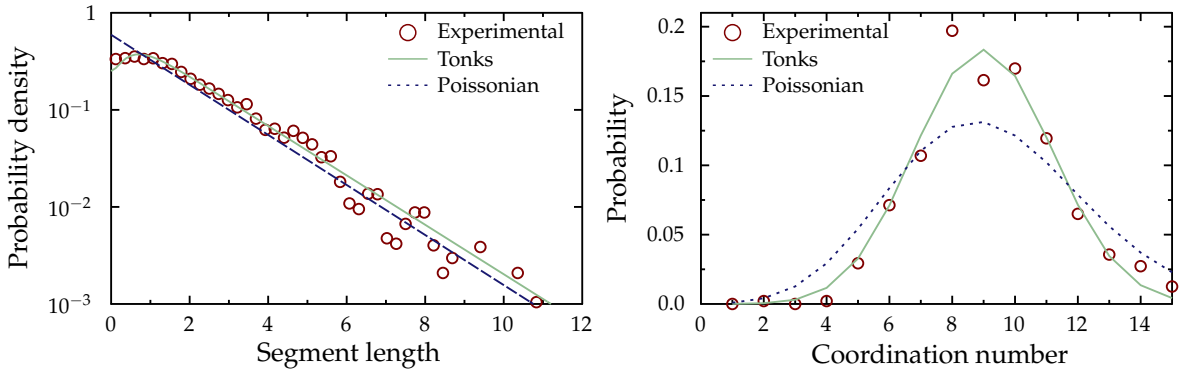

FIGURE 27 Distribution of segment lengths (left side) and coordination number (right side) for a pile of raw short cut spaghetti.

6.2 Geometric availability of fibre ends

As shown in fig. 28a a more detailed analysis of the spatial contact formation on the fibres reveal an abundance of contacts located at the ends of the fibres. It is evident from fig. 19 that this has a drastic effect on the segment lengths. We believe, that this is the most significant finite length effect of random packings of flexible fibres, an issue which we address in Publication V.

6.2.1 End crowding

We considered two theoretical comparisons to see if this end crowding effect could be claimed to be abundant. The most straightforward comparison is that with a 2D Poisson point process in the area of the fibre. This leads, trivially, to a probability of $W/(L+W)$ for a contact along a capsule to be located at either of the spherical caps (ends). The other was a sterically hindered placement of capsules in $\mathbb{R}^3$, which can be solved by considering the excluded volume of the cylinders (fig. 28b). These two cases are compared with the observed fraction of ends contacts as determined by numerical deposition (fig. 28c).

The phenomenon of abundant contacts at the ends of a fibre is also determinable from overlapping soft-core capsules. With soft-core capsules, the mapping of the 'contact' is not as straightforward, but e.g. by defining the contact location as two points of the capsule centre lines closest to each other, the same kind of behaviour is a direct corollary.

Note, that this is not only an effect of the spherical end caps, as cylinders with straight cut edges are trivially overcrowded. By this we mean that the effect is present also for a Poisson point process along the area of the fibre, a feature which is not present for capsules where the overcrowding arises only from a geometric availability.

6.2.2 Segment length

A consequence of this kind of end crowding is the ambiguity of segment lengths. A natural choice for segment length would be the length that defines the solids content,

$$\phi_\mathrm{s} - \rho_\mathrm{f} V_\mathrm{s} = \rho_\mathrm{s} \langle l_\mathrm{s} \rangle A_\mathrm{f} = (2\rho_\mathrm{c} + \rho_\mathrm{f}) \langle l_\mathrm{s} \rangle A_\mathrm{f}, \tag{96}$$

where the correction $\rho_\mathrm{f} V_\mathrm{s}$ takes care of the spherical caps with V_s the combined volume of the capped ends. This kind of definition is a natural extension to line networks, every contact divides the fibre (or the segment) into two parts, thus every fibre consists of $C+1$ segments, including two dangling ends. If such a contact now lies at the end of the fibre, it produces a zero length segment.

An effect of this is evident in the mean segment lengths of the two definitions.

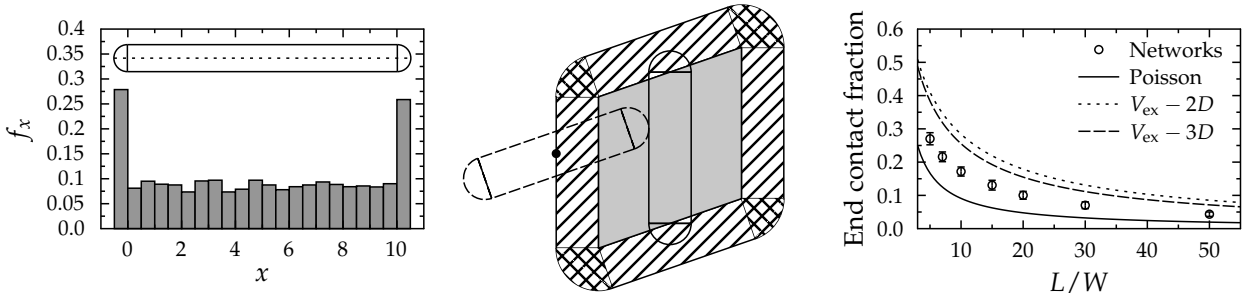

(a) (b) (c)

FIGURE 28 (a) Probability density function f_x for the location of contacts along the extended centre line of a cylinder which is part of a numerically simulated network of capped cylinders of length $L = 10$. Contacts show a significant end crowding effect as the corresponding PDF for a Poisson point process in the fibre area is uniform, when projected onto the extended centre line. (b) A projection of the excluded volume of two capsules consisting of four spherical wedges (grid), four half-cylinders (striped) and a parallelepiped (gray). (c) The observed average end contact fraction $\langle C_e \rangle / \langle C \rangle$ as a function of aspect ratio L/W compared with that of a Poisson point process in the surface area, and a random sterically hindered contact between two capsules.

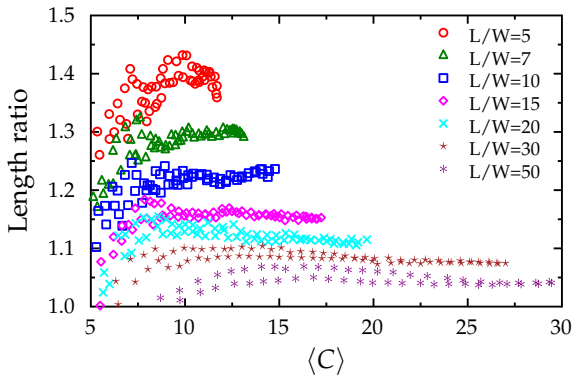

FIGURE 29 The ratio of inter contact distances, excluding all end contacts, with the segment length for numerical networks of a varying aspect ratio.

We show in fig. 29 a comparison between the mean segment length taken over segments containing no end contacts with the mean segment length satisfying the relation in eqn (96).

6.2.3 Long fibre limit

For stiff fibres, in the limit of $L/W \to \infty$, the density ϕ_s goes to 0. Moreover, characteristic length scales of the both segments and void structure diverges. It seems that adding flexibility to the network has quite the opposite effect. For flexible fibres the global properties are not dominated by the aspect ratio, but

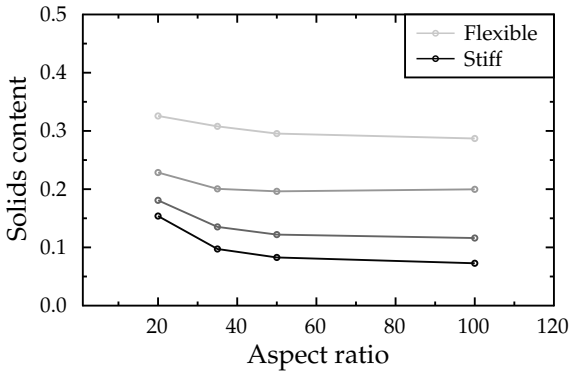

FIGURE 30 Deposited network (in a gravitational field) with fibres of different flexibility and aspect ratio. We notice a convergence of the resulting solids content as a function of aspect ratio.

rather by the local packing and flexure of the constituents. In this case, short fibres cause finite size effects which diminish for an increasing aspect ratio .

This can be observed by making deposition networks with varying aspect ratios but with the same physical parameters for the fibres and the environment and keeping the total mass of the fibres constant. In fig. 30 we show the resulting solids content of this kind of test series for fibres of a varying aspect ratio and flexibility. The results show, that short fibres, regardless of their flexibility, are packed more densely that fibres of larger aspect ratio. This is owing to the fibre geometry, as the excluded volume effect is larger for longer fibres. This effect is however substantially reduced by adding flexibility to the fibres.

The same kind of convergence can be seen in the compression series of rods of a varying aspect ratio. In fig. 31 we show the contact density ρ_c as a function of ϕ_s and $\langle l_s \rangle$ respectively. The geometric availability is evident from the contact density ρ_c as shorter fibres are packed with more contacts. This effect is substantially smaller for longer fibres, and most spectacularly the long rod limit seems to coincide with that of an uncorrelated process.

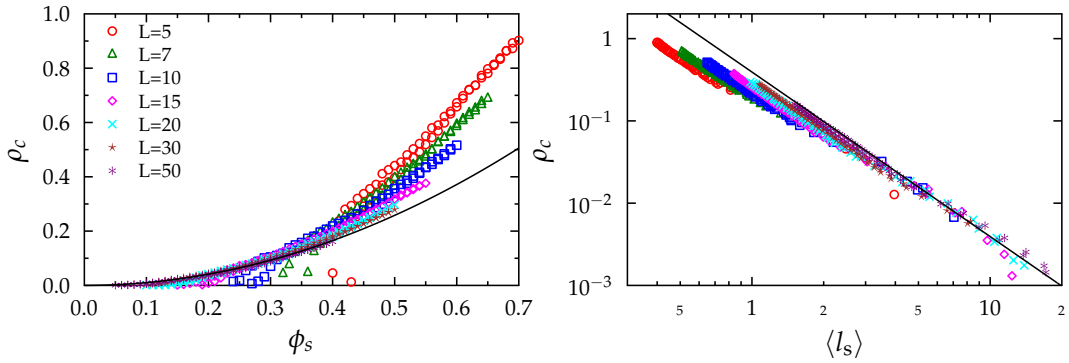

FIGURE 31 Contact density ρ_c as a function of solids content ϕ_s (left side) and mean segment length $\langle l_s \rangle$ (right side). The black line shows the theoretical line for an uncorrelated planar isotropic mass.

6.3 Indirect measurement of network properties

For the indirect measurement of segment length, four sets of networks of different flexibilities were generated using the sequential packing algorithm introduced in Publication I. Two examples of networks of this kind are shown in fig. 32.

As seen from fig. 33a all the initial assumptions did not hold, as the model systematically underestimated the segment length of the sample, i.e. paths were shorter than expected. Although there may be several reasons for this, we found quite good agreement by assuming that fibres were tilted, and thus paths would gain an extra z-component along the segments. Assuming independent distributions of l_s and the 'tilt' angle α, this effective z distance can be given in the form

$$z_{\text{eff}} = \langle l_s \rangle \langle \sin \alpha \rangle + z_0 \langle \sin \alpha \rangle. \tag{97}$$

This provided a tunable calibration parameter. In practice, this parameter was approximately constant, and produced on the average a prefactor of 1.7 ± 0.1 in the measured paths. As shown in fig. 33b, the model is in fairly good agreement with the numerical networks. We belive that the general form given in section 4, now including the steric effects, will substantially enhance the method.

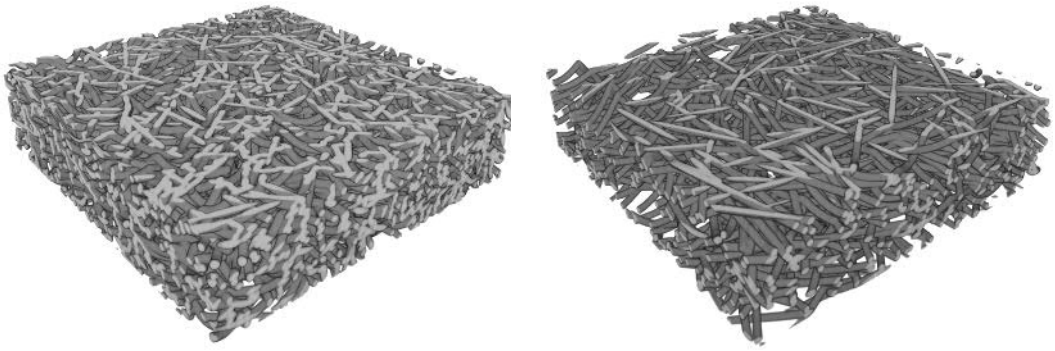

(a) (b)

FIGURE 32 Examples of networks used to calibrate the indirect measuring method. (a) A flexible and (b) stiff network.

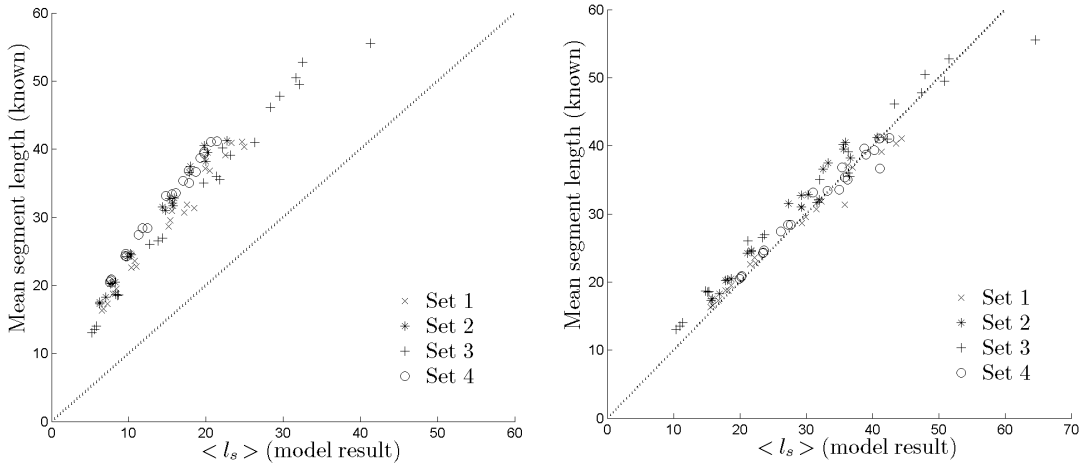

(a) (b)

FIGURE 33 Results of the indirect measurement of segment length. (a) The assumption of a planar network seems to fail, and this model systematically underestimates the mean segment length of the networks. (b) With a correction of the tilt angle of the segment, good agreement with the measured segment lengths is found.

6.4 Steric effects of foam-forming

Steric effects can also arise from other sources than the fibres themselves. One such effect was studied in Publications III and IV in which we studied the resulting microstructure of fibrous networks with added steric effects during the manufacturing of them. This was done by using foam as the carrier liquid during the forming, and it seems that the bubbles in the foam left a trace on the microstructure of the network.

TABLE 3 Fitting parameters for the best fits by eqn (98) on the local thickness of the void space for the numerically generated void space test.

a	μ_1	μ_2	σ_1	σ_2
0.1249	3.8582	0.6803	0.0561	0.6440
0.1503	9.8266	0.6107	0.0439	0.6473

6.4.1 Void size distribution

An example of the effect of foam forming on the void thickness distribution is shown in fig. 34. The effect is evident as an appearance of a clear second local maximum in the void thickness distribution. This kind of bimodal distribution is a common sign of some mixture of random processes, i.e. the observed random variable is unlikely to be a product of a single stochastic process.

Owing to this bimodal feature of the distribution of void thickness, our trial function was a linear combination of two distinct distributions, i.e. a function of the form

$$f_T = aN\left(\mu_1, \sigma_1\right) + \left(1 - a\right) N_{\log}\left(\mu_2, \sigma_2\right), \tag{98}$$

where $N(\mu, \sigma)$ is a Gaussian PDF with mean μ and a standard deviation of σ, and $N_{\log}(\mu, \sigma)$ is a lognormal distribution, where μ and σ represent the conventional position and scale parameters. The reasoning behind this was that the underlying assumption of a log-normal distribution of voids is correct and that foam forming has left some trace on the structure modelled by the inclusion of the second distribution. Of course, the shape of this function is *a priori* unknown, but as the actual bubble size distribution of the foam was measured to be nearly Gaussian, it was a good trial function.

To test the justification of the fitting function we also conducted numerical simulations with added spherical repulsive objects (bubbles). This served two purposes: firstly, and trivialy, that steric effect can modify the structure of the void space, and secondly that we can test the validity of our assumption that a Gaussian fit extracts information about these steric inclusions. An example is given in fig. 35, where we show both the fitted function of eqn (98) and visualisations of the structure. The fitting parameters are shown in table 3. It is evident that the mean of the Gaussian peak describes very well the mean of the added repulsive objects.

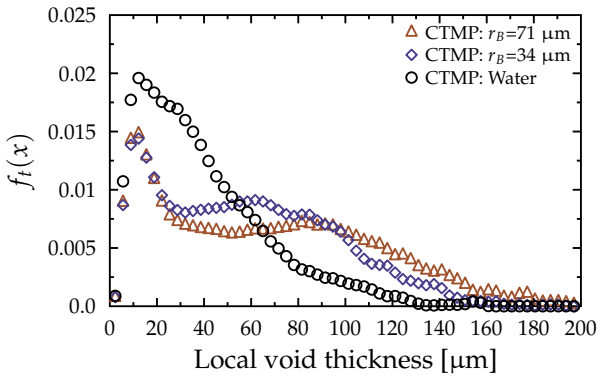

FIGURE 34 Local void thickness distributions for three samples in the CTMP serie. The inclusion of additional steric hindrance in the forming process of fibrous networks affects the structure of the forming network altering the void thickness distribution of the structure. All samples had equal porosity within a 3 % margin.

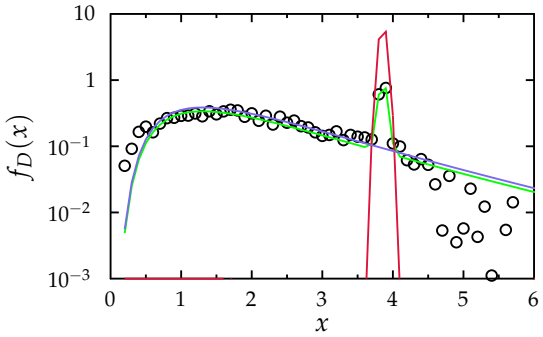

(a) Local thickness, $r_B = 2W$

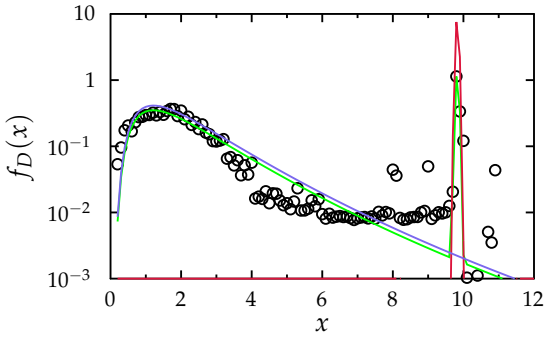

(b) Local thickness, $r_B = 5W$

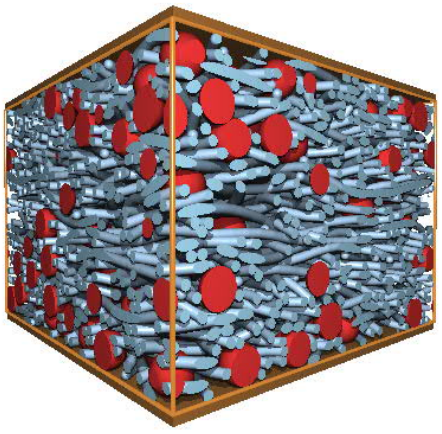

(c) Structure, $r_B = 2W$

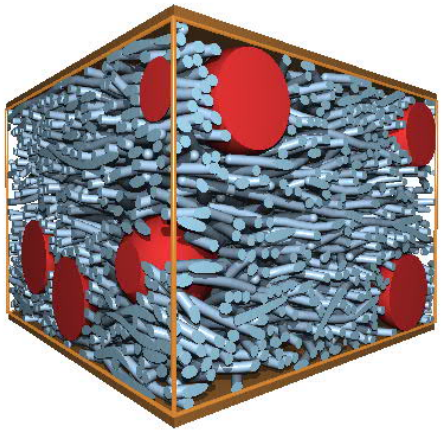

(d) Structure, $r_B = 5W$

FIGURE 35 Fitted combination of a log-normal and a Gaussian void distributions of numerical networks with added spherical voids: Bubble size (a) $r_B = 2W$ and (b) $r_B = 5W$ and the a sample visualisation of the corresponding network structures (c) and (d) respectively. The additional spherical steric hindrances are shown in red.

7 CONCLUSIONS / SUMMARY

The main objectives of this Thesis was to investigate how steric hindrance affects the structure in packing of fibrous (flexible) fibres. This problem was addressed in several different ways, i.e. on a theoretical, a computational and an experimental level. Here we present a summary of the most notable results of our work.

7.1 Summary

The theoretical work resulted in a mathematical way to describe the steric hindrance between he packed objects. This was done by noting the underlying planarity of many deposited structures and modelling the contact formation as a two-sided sterically hindered point process. The model was validated by both experimental and numerical results and seems to be able to, very precisely, describe the observed deviation from earlier theoretical results. Most notably, the contact formation process deviates from an uncorrelated one both in the segment length and coordination number distributions. To simplify, the absence of short segments lies in the inability for two fibres to be next to each other, but contact on opposite sides of a fibre seem to have no such restriction. This steric restriction also decreases to possible configurations of fibres, making the distribution of coordination more narrow.

As a side effect of studying the segment length distributions we found that contacts on the ends of the fibres are abundant. The existence of such effect was validated by both experimental and numerical results, both displaying similar results. The abundance itself can be easily explained by geometric arguments as the ends of the fibres are more available for contact. Its effect, however, leads to some ambiguity of determining the mean segment length, a measure that is linked directly to many physical properties of random networks. Moreover, contacts on ends of fibres are likely to contribute differently to global properties of the

network.

The theoretical model for fibre networks also led to a simple geometric mapping of the point process to form a 3D sterically hindered structure. From this structure, an indirect way of measuring the segment length could be derived. The method, in its pure form, was not suitable for accurate measurements, but with an effective calibration parameter the method was able to predict, with fairly good accuracy, the segment lengths of numerically generated networks.

The numerical study shows, that even if random packing of flexible fibres show finite-length behaviour, the effect scales away very rapidly with increasing aspect ratio. Surprisingly, at larger aspect ratio, both the contact density and the segment length behave in exactly the same way as an uncorrelated process would predict.

The structure of random networks can also be altered by introducing other steric effects than the fibres themselves. This can be achieved in practice by e.g. using foam instead of water as the carrier fluid in the forming process of paper. The resulting effect is evident from the local structure of the resulting void spaces in the network. How this affects the actual network structure is unclear, but one would assume that it may also alter the process of contact formation.

7.2 Outlook

This Thesis is by no means exhaustive on the subject it addresses, and much work is still to be done. Every answered question has led to a new problem. What form should the distribution of the pairwise steric hindrance take? If the mapping of fibres can match many of the relevant properties of the network (ϕ_s, f_{l_s} and ρ_c), can it be used to predict other properties such as permeability or elasticity? Can one work out the carrier fluid of the networks by simply studying the void structure? How does the excessive void space affect the network structure? If the shortest path through a sample can be linked to the segment lengths, can one measure it in faster ways, e.g. by electric conductivity or wave propagation?

Both numerical and experimental work on structural aspects of fibre networks are sparse. μCT provides a very good way for analysing granular particles, as the segmentation process is fairly simple and very accurate. The same cannot be said for flexible objects. A significant amount of work has been invested trying to gain experimental knowledge of soft fibres but, for the time being, proper segmentation methods seem to be out of reach. On the numerical side, both the computational capability and numerical methods are developed rapidly providing fast and accurate assessment tools for theoretical models. On the theoretical level the results, however, provide an evident direction of focus and it would be appealing to explore the effect of the results on existing models of elasticity.

REFERENCES

M. Abramowitz and I. A. Stegun. *Handbook of Mathematical Functions with Formulas, Graphs and Mathematical Tables*. Washington, D.C.: National Bureau of Standards, 1972.

C. K. Aidun and J. R. Clausen. Lattice-boltzmann method for complex flows. *Annual review of fluid mechanics*, 42:439–472, 2010.

R. Bagherzadeh, S. S. Najar, M. Latifi, and L. Kong. A theoretical analysis for fiber contacts in multilayer nanofibrous assemblies. *Textile Research Journal*, page 0040517512456763, 2012.

P. Bak, C. Tang, and K. Wiesenfeld. Self-organized criticality. *Physical Review A*, 38 (1):364–374, 1988.

I. Balberg, C. H. Anderson, S. Alexander, and N. Wagner. Excluded volume and its relation to the onset of percolation. *Physical Review B*, 30(7):3933–3943, 1984.

T. Baradet, J. Haselgrove, and J. Weisel. Three-dimensional reconstruction of fibrin clot networks from stereoscopic intermediate voltage electron microscope images and analysis of branching. *Biophysical Journal*, 68(4):1551–1560, 1995.

C. Barbier, R. Dendievel, and D. Rodney. Numerical study of 3D-compressions of entangled materials. *Computational Materials Science*, 45(3):593–596, 2009a.

C. Barbier, R. Dendievel, and D. Rodney. Role of friction in the mechanics of nonbonded fibrous materials. *Physical Review E*, 80(1):016115, 2009b.

H. G. Barrow, J. M. Tenenbaum, R. C. Bolles, and H. C. Wolf. Parametric correspondence and chamfer matching: Two new techniques for image matching. In *Proceedings of the 5th International Joint Conference on Artificial Intelligence - Volume 2*, IJCAI'77, pages 659–663, San Francisco, CA, USA, 1977. Morgan Kaufmann Publishers Inc.

W. Batchelor and J. He. A new method for determining the relative bonded area. *Tappi Journal*, 4(6):23–28, 2005.

W. Batchelor, R. P. Kibblewhite, and J. He. A new method for measuring rba applied to the page equation for the tensile strength of paper. *Appita Journal*, 61 (4):302–306, 2008.

G. A. Baum. The elastic properties of paper: a review. In *IPST Technical Paper Series*, number 145. The institute of paper chemistyr, Appelton, Wisconsin, 1984.

J. Bear. *Dynamics of fluids in porous media*. Courier Corporation, 2013.

J. Bender, K. Erleben, and J. Trinkle. Interactive simulation of rigid body dynamics in computer graphics. *Computer Graphics Forum*, 33(1):246–270, 2013.

M. Bergou, M. Wardetzky, S. Robinson, B. Audoly, and E. Grinspun. Discrete elastic rods. *ACM Transactions on Graphics*, 27(3):63:1–63:12, 2008.

L. Berhan and A. M. Sastry. Modeling percolation in high-aspect-ratio fiber systems. i. soft-core versus hard-core models. *Physical Review E*, 75(4):041120, 2007.

L. Berhan, Y. B. Yi, A. M. Sastry, E. Munoz, M. Selvidge, and R. Baughman. Mechanical properties of nanotube sheets: Alterations in joint morphology and achievable moduli in manufacturable materials. *Journal of Applied Physics*, 95(8):4335–4345, 2004.

J. D. Bernal. The bakerian lecture, 1962. the structure of liquids. *Proceedings of the Royal Society of London. Series A, Mathematical and Physical Sciences*, 280(1382): 299–322, 1964.

F. Bertails-Descoubes, F. Cadoux, G. Daviet, and V. Acary. A nonsmooth newton solver for capturing exact coulomb friction in fiber assemblies. *ACM Transactions on Graphics*, 30(1):6:1–6:14, 2011.

S. Blacher, A. Léonard, B. Heinrichs, N. Tcherkassova, F. Ferauche, M. Crine, P. Marchot, E. Loukine, and J.-P. Pirard. Image analysis of x-ray microtomograms of pd–ag/sio2 xerogel catalysts supported on al2o3 foams. *Colloids and Surfaces A: Physicochemical and Engineering Aspects*, 241(1):201–206, 2004.

J. Blouwolff and S. Fraden. The coordination number of granular cylinders. *Europhysics Letters*, 76(6):1095, 2006.

P. Bolhuis and D. Frenkel. Tracing the phase boundaries of hard spherocylinders. *The Journal of Chemical Physics*, 106(2):666–687, 1997.

G. Borgefors. Distance transformations in digital images. *Computer Vision, Graphics, and Image Processing*, 34(3):344–371, 1986.

R. Bridson, R. Fedkiw, and J. Anderson. Robust treatment of collisions, contact and friction for cloth animation. *ACM Transactions on Graphics*, 21(3):594–603, 2002.

C. P. Broedersz, C. Storm, and F. C. MacKintosh. Nonlinear elasticity of composite networks of stiff biopolymers with flexible linkers. *Physical Review Letters*, 101 (11):118103, 2008.

C. P. Broedersz, X. Mao, T. C. Lubensky, and F. C. MacKintosh. Criticality and isostaticity in fibre networks. *Nature Physics*, 7(12):983–988, 2011.

C. P. Broedersz, M. Sheinman, and F. C. MacKintosh. Filament-length-controlled elasticity in 3D fiber networks. *Physical Review Letters*, 108(7):078102, 2012.

G. A. Buxton and N. Clarke. "Bending to Stretching" transition in disordered networks. *Physical Review Letters*, 98(23):238103, 2007.

Q. Cao and J. A. Rogers. Ultrathin films of single-walled carbon nanotubes for electronics and sensors: A review of fundamental and applied aspects. *Advanced Materials*, 21(1):29–53, 2009.

L. A. Carlsson and T. Lindstrom. A shear-lag approach to the tensile strength of paper. *Composites Science and Technology*, 65(2):183–189, 2005.

P. C. Carman. Fluid flow through granular beds. *Transactions-Institution of Chemical Engineeres*, 15:150–166, 1937.

M. E. Cates, J. P. Wittmer, J.-P. Bouchaud, and P. Claudin. Jamming, force chains, and fragile matter. *Physical Review Letter*, 81(9):1841–1844, 1998.

S. Chen and G. D. Doolen. Lattice boltzmann method for fluid flows. *Annual review of fluid mechanics*, 30(1):329–364, 1998.

X. Cheng, A. Sastry, and B. Layton. Transport in stochastic fibrous networks. *Journal of engineering materials and technology*, 123(1):12–19, 2001.

E. C. Childs and N. Collis-George. The permeability of porous materials. *Proceedings of the Royal Society A: Mathematical, Physical and Engineering Sciences*, 201 (1066):392–405, 1950.

H. Corte and E. H. Lloyd. Fluid flow through paper and sheet structure. In *Consolidation of the Paper Web Trans. IIIrd Fund. Res. Symp*, pages 981–1009, 1965.

E. I. Corwin, H. M. Jaeger, and S. R. Nagel. Structural signature of jamming in granular media. *Nature*, 435(7045):1075–1078, 2005.

H. L. Cox. The elasticity and strength of paper and other fibrous materials. *British Journal of Applied Physics*, 3(3):72–79, 1952.

M. W. Crofton. On the theory of local probability, applied to straight lines drawn at random in a plane; the methods used being also extended to the proof of certain new theorems in the integral calculus. *Philosophical Transactions of the Royal Society of London*, 158(0):181–199, 1868.

P. A. Cundall and O. D. L. Strack. A discrete numerical model for granular assemblies. *Géotechnique*, 29(1):47–65, 1979.

F. Dalmas, R. Dendievel, L. Chazeau, J.-Y. Cavaillé, and C. Gauthier. Carbon nanotube-filled polymer composites. numerical simulation of electrical conductivity in three-dimensional entangled fibrous networks. *Acta Materialia*, 54(11): 2923–2931, 2006.

G. Daviet, F. Bertails-Descoubes, and L. Boissieux. A hybrid iterative solver for robustly capturing coulomb friction in hair dynamics. *ACM Transactions on Graphics*, 30(6):139:1–139:12, 2011.

P. G. de Gennes. Granular matter: a tentative view. *Reviews of Modern Physics*, 71: S374–S382, 1999.

M. Deng. *Paper, An Engineered Stochastic Structure*. TAPPI Press, Atlanta, 1994.

D. Denisov, Y. Villanueva, K. Lőrincz, S. May, and R. Wijngaarden. Relation between self-organized criticality and grain aspect ratio in granular piles. *Physical Review E*, 85(5):051309, 2012.

K. Desmond and S. V. Franklin. Jamming of three-dimensional prolate granular materials. *Physical Review E*, 85(5):031306, 2006.

B. A. DiDonna and A. J. Levine. Filamin cross-linked semiflexible networks: Fragility under strain. *Physical Review Letter*, 97(6):068104, 2006.

M. Dijkstra, R. v. Roij, and R. Evans. Wetting and capillary nematization of a hard-rod fluid: A simulation study. *Physical Review E*, 63(5):051703, 2001.

T. Dillard, F. N'guyen, E. Maire, L. Salvo, S. Forest, Y. Bienvenu, J.-D. Bartout, M. Croset, R. Dendievel, and P. Cloetens. 3D quantitative image analysis of open-cell nickel foams under tension and compression loading using x-ray microtomography. *Philosophical Magazine*, 85(19):2147–2175, 2005.

C. Dodson. Fibre crowding, fibre contacts and fibre flocculation. *Tappi Journal*, 79 (9):211–216, 1996.

C. T. J. Dodson. On the distribution of pore heights in layered random fibre networks. *Source internet (http://www. maths. manchester. ac. uk/kd/PREPRINTS/poreht. pdf)*, 2000.

A. Donev, I. Cisse, D. Sachs, E. A. Variano, F. H. Stillinger, R. Connelly, S. Torquato, and P. M. Chaikin. Improving the density of jammed disordered packings using ellipsoids. *Science*, 303(5660):990–993, 2004.

R. Dougherty and K.-H. Kunzelmann. Computing local thickness of 3D structures with imagej. *Microscopy and Microanalysis*, 13(S02):1678–1679, 2007.

F. Du, R. C. Scogna, W. Zhou, S. Brand, J. E. Fischer, and K. I. Winey. Nanotube networks in polymer nanocomposites: rheology and electrical conductivity. *Macromolecules*, 37(24):9048–9055, 2004.

S. J. Eichhorn and W. W. Sampson. Statistical geometry of pores and statistics of porous nanofibrous assemblies. *Journal of The Royal Society Interface*, 2(4):309–318, 2005.

W. G. Ellenbroek, Z. Zeravcic, W. van Saarloos, and M. van Hecke. Non-affine response: Jammed packings vs. spring networks. *Europhysics Letters*, 87(3):34004, 2009.

J. A. Elliott, A. H. Windle, J. R. Hobdell, G. Eeckhaut, R. J. Oldman, W. Ludwig, E. Boller, P. Cloetens, and J. Baruchel. In-situ deformation of an open-cell flexible polyurethane foam characterised by 3d computed microtomography. *Journal of Materials Science*, 37(8):1547–1555, 2002.

L. A. Feldkamp, L. C. Davis, and J. W. Kress. Practical cone-beam algorithm. *J. Opt. Soc. Am. A*, 1(6):612–619, 1984.

D. A. Fletcher and R. D. Mullins. Cell mechanics and the cytoskeleton. *Nature*, 463 (7280):485–492, 2010.

V. Frette, K. Christensen, A. Malthe-Sørenssen, J. Feder, T. Jøssang, and P. Meakin. Avalanche dynamics in a pile of rice. *Nature*, 379(6560):49–52, 1996.

R. Goldenthal, D. Harmon, R. Fattal, M. Bercovier, and E. Grinspun. Efficient simulation of inextensible cloth. *ACM Transactions on Graphics*, 26(3), 2007.

R. C. Gonzales and R. E. Woods. *Digital Image Processing*. Prentice-Hall, Inc, New Jersey, 2nd edition, 1993.

S. Goudsmit. Random distribution of lines in a plane. *Reviews of Modern Physics*, 17(2–3):321–322, 1945.

I. S. Gradshteyn and I. M. Ryzhik. *Table of Integrals, Series, and Products*. Academic Press, London, 1965.

J. He, W. J. Batchelor, and R. E. Johnston. A microscopic study of fibre-fibre contacts in paper. *Appita Journal*, 57:292–298, 2004.

J. He, W. J. Batchelor, and R. E. Johnston. An analytical model for number of fibre-fibre contacts in paper and expressions for relative bonded area (rba). *Journal of Materials Science*, 42(2):522–528, 2007.

D. A. Head, A. J. Levine, and F. C. MacKintosh. Deformation of cross-linked semiflexible polymer networks. *Physical Review Letter*, 91(10):108102, 2003.

E. K. O. Hellen and M. J. Alava. Porous structure of thick fiber webs. *Journal of Applied Physics*, 81:6425–6431, 1997.

E. K. O. Hellen, J. A. Ketoja, K. J. Niskanen, and M. J. Alava. Diffusion through fibre networks. *Journal of pulp and paper science*, 28(2):55–62, 2002.

C. Heussinger and E. Frey. Floppy modes and nonaffine deformations in random fiber networks. *Physical Review Letter*, 97(10):105501, 2006.

C. Heussinger, B. Schaefer, and E. Frey. Nonaffine rubber elasticity for stiff polymer networks. *Physical Review E*, 76(3):031906, 2007.

J. J. L. Higdon and G. D. Ford. Permeability of three-dimensional models of fibrous porous media. *Journal of Fluid Mechanics*, 308:341–361, 1996.

T. Hildebrand and P. Rüegsegger. A new method for the model-independent assessment of thickness in three-dimensional images. *Journal of microscopy*, 185 (1):67–75, 1997.

L. Hu, D. Hecht, and G. Grüner. Percolation in transparent and conducting carbon nanotube networks. *Nano Letters*, 4(12):2513–2517, 2004.

L. Hu, M. Pasta, F. L. Mantia, L. Cui, S. Jeong, H. D. Deshazer, J. W. Choi, S. M. Han, and Y. Cui. Stretchable, porous, and conductive energy textiles. *Nano letters*, 10(2):708–714, 2010.

X. Huang, Q. Wang, W. Zhou, D. Deng, Y. Zhao, D. Wen, and J. Li. Morphology and transport properties of fibrous porous media. *Powder Technology*, 283:618–626, 2015.

E. M. Huisman, T. van Dillen, P. R. Onck, and E. Van der Giessen. Three-dimensional cross-linked f-actin networks: Relation between network architecture and mechanical behavior. *Physical Review Letter*, 99:208103, 2007.

W. Ingmanson and E. Thode. Factors contributing to the strength of a sheet of paper. ii. relative bonded area. *Tappi Journal*, 42(1):83–93, 1959.

G. W. Jackson and D. F. James. The permeability of fibrous porous media. *The Canadian Journal of Chemical Engineering*, 64(3):364–374, 1986.

H. M. Jaeger, S. R. Nagel, and R. P. Behringer. Granular solids, liquids, and gases. *Reviews of Modern Physics*, 68(4):1259, 1996.

S. Jockenhoevel and T. C. Flanagan. *Cardiovascular tissue engineering based on fibrin-gel-scaffolds*. INTECH Open Access Publisher, 2011.

A. C. Kak and M. Slaney. *Principles of Computerized Tomographic Imaging*. IEEE PRESS, Electronic copy, 1999.

O. Kallmes and G. Bernier. The structure of paper, iii. the absolute, relative and maximum bonded areas of random fiber networks. *Tappi Journal*, 45(11):867–72, 1962.

O. Kallmes and O. Corte. Structure of paper i. the statistical geometry of an ideal two dimensional fiber network. *Tappi Journal*, 43:737–752, 1960.

O. Kallmes and O. Corte. Structure of paper ii. the statistical geometry of a multiplanar fiber network. *Tappi Journal*, 44:519–528, 1961.

Y. Kantor and M. Kardar. One-dimensional gas of hard needles. *Physical Review E*, 79:041109, 2009.

G. Kerckhofs, J. Schrooten, T. Van Cleynenbreugel, S. V. Lomov, and M. Wevers. Validation of x-ray microfocus computed tomography as an imaging tool for porous structures. *Review of Scientific Instruments*, 79(1):013711, 2008.

T. Komori and M. Itoh. A modified theory of fiber contact in general fiber assemblies. *Textile Research Journal*, 64(9):519–528, 1994.

T. Komori and K. Makishima. Number of fiber-to-fiber contacts in general fiber assemblies. *Textile Research Journal*, 47(13):13–17, 1977.

A. Koponen, D. Kandhai, M. Alava, A. Heokstra, M. Kataja, K. Niskanen, P. Stoot, and J. timonen. Permeability of three-dimensional random fiber webs. *Physical Review Letter*, 80:716–719, 1998.

J. Kozeny. *Über kapillare Leitung des Wassers im Boden:(Aufstieg, Versickerung und Anwendung auf die Bewässerung)*. Hölder-Pichler-Tempsky, 1927.

A. Kulachenko and T. Uesaka. Direct simulations of fiber network deformation and failure. *Mechanics of Materials*, 51:1–14, 2012.

A. V. Kyrylyuk, M. A. van de Haar, L. Rossi, A. Wouterse, and A. P. Philipse. Isochoric ideality in jammed random packings of non-spherical granular matter. *Soft Matter*, 7(5):1671–1674, 2011.

M. Latva-Kokko and J. Timonen. Rigidity of random networks of stiff fibers in the low-density limit. *Physical Review E*, 64(6):066117, 2001.

M. Latva-Kokko, J. Mäkinen, and J. Timonen. Rigidity transition in two-dimensional random fiber networks. *Physical Review E*, 63(4):046113, 2001.

A. J. Lawrence. Dependency of intervals between events in superposition processes. *Journal of The Royal Statistical Society. Series B (Methodological)*, 35(2): 306–315, 1973.

H. N. W. Lekkerkerker, P. Coulon, and v. d. R. Haegen. On the isotropic-liquid crystal phase separation in a solution of rodlike particles of different lengths. *The Journal of Chemical Physics*, 80(7):3427–3433, 1984.

S. B. Lindström and T. Uesaka. Simulation of the motion of flexible fibers in viscous fluid flow. *Physics of Fluids*, 19(11):113307, 2007.

S. B. Lindström and T. Uesaka. Particle-level simulation of forming of the fiber network in papermaking. *International Journal of Engineering Science*, 46(9):858–876, 2008.

J. Lux, A. Ahmadi, C. Gobbé, and C. Delisée. Macroscopic thermal properties of real fibrous materials: Volume averaging method and 3d image analysis. *International Journal of Heat and Mass Transfer*, 49(11):1958–1973, 2006.

E. Maire, J.-Y. Buffiere, L. Salvo, J. J. Blandin, W. Ludwig, and J. M. Letang. On the application of x-ray microtomography in the field of materials science. *Advanced Engineering Materials*, 3(8):539–546, 2001.

E. Maire, A. Fazekas, L. Salvo, R. Dendievel, S. Youssef, P. Cloetens, and J. M. Letang. X-ray tomography applied to the characterization of cellular materials. related finite element modeling problems. *Composites Science and Technology*, 63 (16):2431–2443, 2003.

T. S. Majmudar and R. P. Behringer. Contact force measurements and stress-induced anisotropy in granular materials. *Nature*, 435(7045):1079–1082, 2005.

T. Marshall. A relation between permeability and size distribution of pores. *Journal of Soil Science*, 9(1):1–8, 1958.

C. Marulier, P. J. J. Dumont, L. Orgéas, D. Caillerie, and S. R. du Roscoat. Towards 3d analysis of pulp fibre networks at the fibre and bond levels. *Nordic Pulp and Paper Research Journal*, 27(2):245–255, 2012.

K. Mattila, T. Puurtinen, J. Hyväluoma, R. Surmas, M. Myllys, T. Turpeinen, F. Robertsén, J. Westerholm, and J. Timonen. A prospect for computing in porous materials research: very large fluid flow simulations. *Journal of Computational Science*, 12:62–76, 2016.

O. Medalia, I. Weber, A. S. Frangakis, D. Nicastro, G. Gerisch, and W. Baumeister. Macromolecular architecture in eukaryotic cells visualized by cryoelectron tomography. *Science*, 298(5596):1209–1213, 2002.

A. Miettinen, C. L. L. Hendriks, G. Chinga-Carrasco, E. K. Gamstedt, and M. Kataja. A non-destructive x-ray microtomography approach for measuring fibre length in short-fibre composites. *Composites Science and Technology*, 72(15):1901–1908, 2012.

R. E. Miles. Random polygons determined by random lines in a plane. *Proceedings of the National Academy of Sciences of the United States of America*, 52(4):901–907, 1964.

R. Montanini. Measurement of strain rate sensitivity of aluminium foams for energy dissipation. *International Journal of Mechanical Sciences*, 47(1):26–42, 2005.

M. D. Montminy, A. R. Tannenbaum, and C. W. Macosko. The 3d structure of real polymer foams. *Journal of Colloid and Interface Science*, 280(1):202–211, 2004.

R. Moreno-Atanasio, R. A. Williams, and X. Jia. Combining x-ray microtomography with computer simulation for analysis of granular and porous materials. *Particuology*, 8(2):81–99, 2010.

A. Nabovati, E. W. Llewellin, and A. C. Sousa. A general model for the permeability of fibrous porous media based on fluid flow simulations using the lattice boltzmann method. *Composites Part A: Applied Science and Manufacturing*, 40(6): 860–869, 2009.

W. Nan, Y. Wang, Y. Ge, and J. Wang. Effect of shape parameters of fiber on the packing structure. *Powder Technology*, 261:210–218, 2014.

B. Neckář and S. Ibrahim. Theoretical approach for determining pore characteristics between fibers. *Textile research journal*, 73(7):611–619, 2003.

L. Nilsson and S. Stenström. A study of the permeability of pulp and paper. *International Journal of Multiphase Flow*, 23(1):131–153, 1997.

K. Niskanen, N. Nilsen, E. Hellen, and M. Alava. KCL-PAKKA: Simulation of the 3d structure of paper. In *The Fundamentals of Papermaking Materials, The Eleventh Fundamental Research Symposium*, pages 1177–1213, 1997.

K. J. Niskanen and M. J. Alava. Planar random networks with flexible fibers. *Physical Review Letter*, 73(25):3475–3478, 1994.

L. Onsager. The effects of shape on the interaction of colloidal particles. *Annals of the New York Academy of Sciences*, 51(4):627–659, 1949.

D. H. Page. A theory for the tensile strength of paper. *Tappi Journal*, 52:674–681, 1969.

D. H. Page, R. S. Seth, and J. H. Degrace. The elastic modulus of paper. part i. the controlling mechanisms. *Tappi Journal*, 62(9):99–102, 1979.

N. Pan. A modified analysis of the microstructural characteristics of general fiber assemblies. *Textile Research Journal*, 63(6):336–345, 1993.

N. Pan. Analytical characterization of the anisotropy and local heterogeneity of short fiber composites: Fiber fraction as a variable. *Journal of Composite Materials*, 28(16):1500–1531, 1994.

N. Pan, J.-H. He, and J. Yu. Fibrous materials as soft matter. *Textile research journal*, 77(4):205–213, 2007.

A. P. Philipse. The random contact equation and its implication for (colloidal) rods in packings, suspensions, and anisotropic powders. *Langmuir*, 12:1127–1133, 1996.

R. C. Picu. Mechanics of random fiber networks: a review. *Soft Matter*, 7(15): 6768–6785, 2011.

W. R. Purcell. Capillary pressures – their measurement using mercury and the calculation of permeability therefrom. *Journal of Petroleum Technology*, 1(02): 39–48, 1949.

M. J. Puttock and E. G. Thwaite. *Elastic compression of spheres and cylinders at point and line contact*. Commonwealth Scientific and Industrial Research Organization Melbourne, VIC, Australia, 1969.

E. Remy and T. E. Optimizing 3d chamfer masks with norm constraints. In *XIIth Fundamental Research Symposium*, pages 39–56, 2000.

P. Richard, P. Philippe, F. Barbe, S. Bourlès, X. Thibault, and D. Bideau. Analysis by x-ray microtomography of a granular packing undergoing compaction. *Physical Review E*, 68(2):020301, 2003.

A. Robledo and J. S. Rowlinson. The distribution of hard rods on a line of finite length. *Molecular Physics*, 58(4):711–721, 1986.

D. Rodney, M. Fivel, and R. Dendievel. Discrete modeling of the mechanics of entangled materials. *Physical Review Letter*, 95(10):108004, 2005.

A. S. Saada. *Elasticity: Theory and Applications*. J. Ross Publishing, 2009.

L. Salvo, P. Cloetens, E. Maire, S. Zabler, J. Blandin, J.-Y. Buffière, W. Ludwig, E. Boller, D. Bellet, and C. Josserond. X-ray micro-tomography an attractive characterisation technique in materials science. *Nuclear instruments and methods in physics research section B: Beam interactions with materials and atoms*, 200:273–286, 2003.

W. W. Sampson. The statistical geometry of fractional contact area in random fibre networks. *Journal of pulp and paper science*, 29(12):412–416, 2003.

W. W. Sampson. A model for fibre contact in planar fibre networks. *Journal of Material Science*, 39:2775–2781, 2004.

W. W. Sampson and J. Sirviö. The statistics of interfibre contact in random fibre networks. *Journal of pulp and paper science*, 31(3):127–131, 2005.

V. K. Sangwan, R. P. Ortiz, J. M. P. Alaboson, J. D. Emery, M. J. Bedzyk, L. J. Lauhon, T. J. Marks, and M. C. Hersam. Fundamental performance limits of carbon nanotube thin-film transistors achieved using hybrid molecular dielectrics. *Acs Nano*, 6(8):7480–7488, 2012.

A. Scheidegger. *The physics of flow through porous media*. Toronto: University of Toronto, 1957.

G. T. Seidler, G. Martinez, L. H. Seeley, K. H. Kim, E. A. Behne, S. Zaranek, B. D. Chapman, S. M. Heald, and D. L. Brewe. Granule-by-granule reconstruction of a sandpile from x-ray microtomography data. *Physical Review E*, 62(6):8175–8181, 2000.

J. Shäfer, S. Dippel, and D. E. Wolf. Force schemes in simulations of granular materials. *Journal de physique I*, 6(1):5–20, 1996.

H. Shen, S. Nutt, and D. Hull. Direct observation and measurement of fiber architecture in short fiber-polymer composite foam through micro-ct imaging. *Composites Science and Technology*, 64(13):2113–2120, 2004.

D. A. Singer. Lectures on elastic curves and rods. *AIP Conference Proceedings*, 1002 (1):3–32, 2008.

E. S. Snow, J. P. Novak, P. M. Campbell, and D. Park. Random networks of carbon nanotubes as an electronic material. *Applied Physics Letters*, 82(13):2145–2147, 2003.

P. Soltani, M. S. Johari, and M. Zarrebini. Effect of 3d fiber orientation on permeability of realistic fibrous porous networks. *Powder Technology*, 254:44–56, 2014.

C. Song, P. Wang, and H. A. Makse. A phase diagram for jammed matter. *Nature*, 453(7195):629–632, 2008.

J. Spillmann and M. Teschner. Corde: Cosserat rod elements for the dynamic simulation of one-dimensional elastic objects. In *Proceedings of the 2007 ACM SIGGRAPH/Eurographics Symposium on Computer Animation*, SCA '07, pages 63–72, 2007. ISBN 978-1-59593-624-0.

J. Spillmann and M. Teschner. An adaptive contact model for the robust simulation of knots. *Computer Graphics Forum*, 27(2):497–506, 2008.

S. R. Stock. X-ray microtomography of materials. *International Materials Reviews*, 44(4):141–164, 1999.

S. R. Stock. *MicroComputed Tomography, Methology and Applications*. CRC Press, 2009.

C. Storm, J. J. Pastore, F. C. MacKintosh, T. C. Lubensky, and P. A. Janmey. Nonlinear elasticity in biological gels. *Nature*, 435(7039):191–194, 2005.

T. Stylianopoulos, A. Yeckel, J. J. Derby, X.-J. Luo, M. S. Shephard, E. A. Sander, and V. H. Barocas. Permeability calculations in three-dimensional isotropic and oriented fiber networks. *Physics of Fluids*, 20(12):123601, 2008.

G. Subramanian and C. R. Picu. Mechanics of three-dimensional, nonbonded random fiber networks. *Physical Review E*, 83(5):056120, 2011.

L. Switzer and D. J. Klingenberg. Flocculation in simulations of sheared fiber suspensions. *International Journal of Multiphase Flow*, 30(1):67–87, 2004.

L. H. Switzer, D. J. Klingenberg, and C. T. Scott. Handsheet formation and mechanical testing via fiber-level simulations. *Nordic Pulp and Paper Research Journal*, 19 (4):434–439, 2004.

J. J. Sylvester. On a funicular solution of Buffon's "problem of the needle" in its most general form. *Acta Mathematica*, 14(1):185–205, 1890.

M. Teschner, B. Heidelberger, M. Müller, D. Pomerantes, and M. H. Gross. Optimized spatial hashing for collision detection of deformable objects. In *VMV*, volume 3, pages 47–54, 2003.

S. Toll. Packing mechanics of fiber reinforcements. *Polymer Engineering and Science*, 38:1337–1350, 1998.

M. M. Tomadakis and T. J. Robertson. Viscous permeability of random fiber structures: comparison of electrical and diffusional estimates with experimental and analytical results. *Journal of Composite Materials*, 39(2):163–188, 2005.

L. Tonks. The complete equation of state of one, two and three-dimensional gases of hard elastic spheres. *Physical Review*, 50:955–963, 1936.

S. Torquato. *Random Heterogeneous Materials*. Springer, 2001.

S. Torquato, T. M. Truskett, and P. G. Debenedetti. Is random close packing of spheres well defined? *Physical review letters*, 84(10):2064–2067, 2000.

D. Tsarouchas and A. E. Markaki. Extraction of fibre network architecture by x-ray tomography and prediction of elastic properties using an affine analytical model. *Acta Materialia*, 59(18):6989–7002, 2011.

H. Turbell. *Cone-beam reconstruction using Filtered Backprojection*. PhD thesis, Institute of Technology, University of Linköping, 2001.

T. Turpeinen. *Analysis of microtomographic images of porous heterogeneous materials*. PhD thesis, University of Jyväskylä, 2015.

T. Turpeinen, M. Myllys, P. Kekalainen, and J. Timonen. Interface detection using a quenched-noise version of the edwards-wilkinson equation. *Image Processing, IEEE Transactions on*, 24(12):5696–5705, 2015.

C. M. van Wyk. Note on the compressibility of wool. *The Journal of The Textile Industry*, 37:285–292, 1946.

C. Vega and S. Lago. A fast algorithm to evaluate the shortest distance between rods. *Computers & chemistry*, 18(1):55–59, 1994.

C. W. Wang and A. M. Sastry. Structure, mechanics and failure of stochastic fibrous networks: Part ii – network simulations and application. *Journal of Engineering Materials and Technology*, 122(4):460–468, 2000.

J. Wilhelm and E. Frey. Elasticity of stiff polymer networks. *Physical Review Letter*, 91(10):108103, 2003.

S. R. Williams and A. P. Philipse. Random packings of spheres and spherocylinders simulated by mechanical contraction. *Physical Review E*, 67(5):051301, 2003.

A. Wouterse, S. Luding, and A. P. Philipse. On contact numbers in random rod packings. *Granular Matter*, 11(3):169–177, 2009.

X.-F. Wu and Y. A. Dzenis. Elasticity of planar fiber networks. *Journal of Applied Physics*, 98(9):093501, 2005.

Y. B. Yi, L. Berhan, and A. M. Sastry. Statistical geometry of random fibrous networks, revisited: waviness, dimensionality, and percolation. *Journal of Applied physics*, 96(3):1318–1327, 2004.

P. D. Yurchenco and G. C. Ruben. Basement membrane structure in situ: evidence for lateral associations in the type iv collagen network. *The Journal of Cell Biology*, 105(6):2559–2568, 1987.

H. P. Zhu, Z. Y. Zhou, R. Y. Yang, and A. B. Yu. Discrete particle simulation of particulate systems: theoretical developments. *Chemical Engineering Science*, 62 (13):3378–3396, 2007.

J. A. Åström, J. P. Mäkinen, M. J. Alava, and J. Timonen. Elasticity of poissonian fiber networks. *Physical Review E*, 61(5):5550–5556, 2000a.

J. A. Åström, J. P. Mäkinen, H. Hirvonen, and J. Timonen. Stiffness of compressed fiber mats. *Journal of Applied Physics*, 8:5056–5061, 2000b.